Norsk institutt for luftforskning
Norwegian Institute for Air Research

Towards better exploitation of Satellite data for monitoring Air Quality in Norway using downscaling techniques (SAT4AQN)

Final project report

Kerstin Stebel, Philipp Schneider, Arve Kylling and Tove Svendby

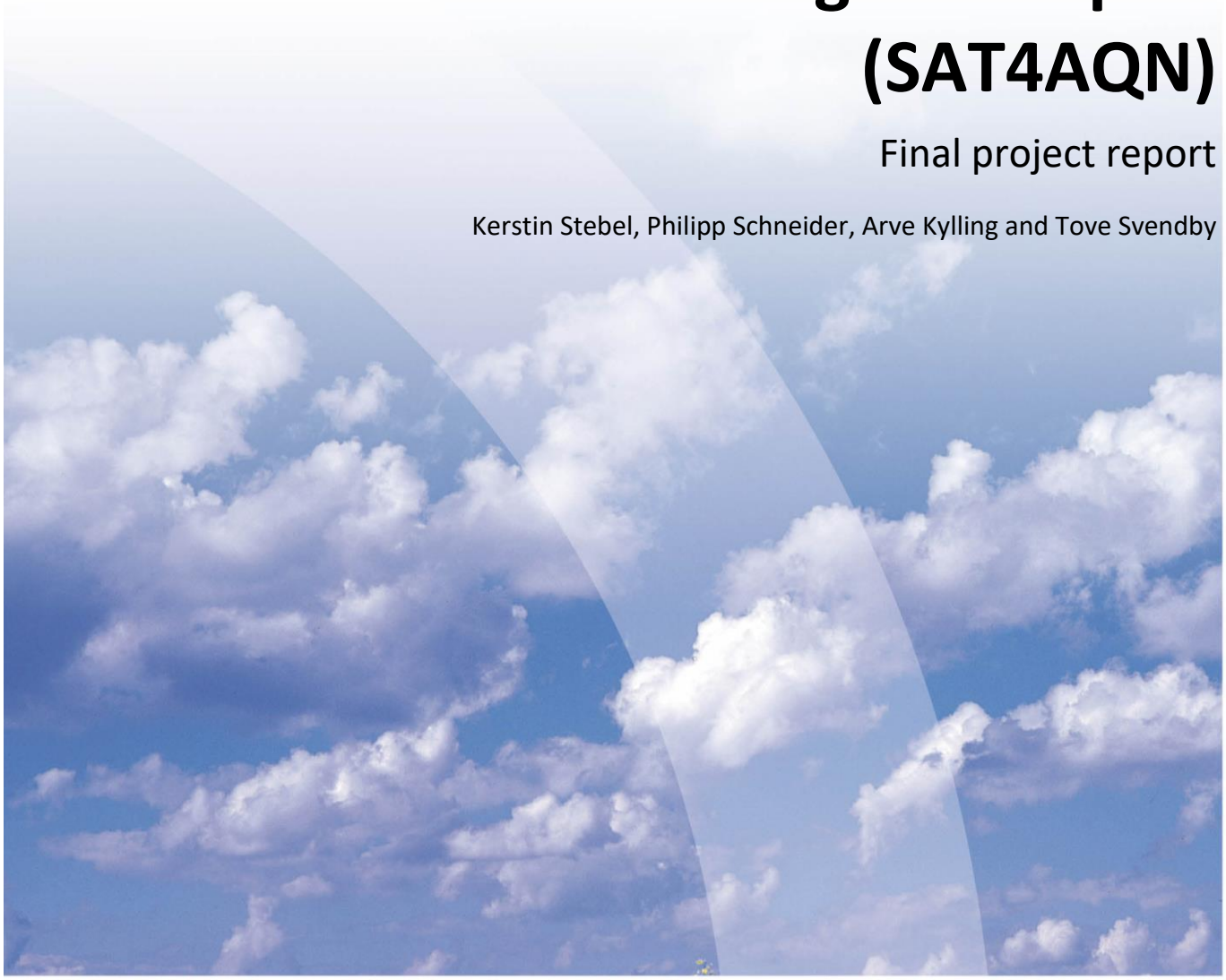

NILU report 2/2019

NILU report 2/2019	ISBN: 978-82-425-2963-3 ISSN: 2464-3327	CLASSIFICATION: A – Unclassified (open report)
DATE 02-06-2020	SIGNATURE OF RESPONSIBLE PERSON Ole-Anders Braathen, Deputy Director	NUMBER OF PAGES 39

TITLE	PROJECT LEADER
Towards better exploitation of Satellite data for monitoring Air Quality in Norway using downscaling techniques (SAT4AQN) Final project report	Kerstin Stebel
	NILU PROJECT NO. 117010
AUTHOR(S) Kerstin Stebel, Philipp Schneider, Arve Kylling and Tove Svendby	QUALITY CONTROLLER Kjetil Tørseth
REPORT PREPARED FOR Norsk Romsenter, Postboks 113 Skøyen, 0212 Oslo Att.: Maria Høegh Berdahl	CONTRACT REF. NRS-contract number: NIT.05.16.5

ABSTRACT

The main goal for the “Towards better exploitation of Satellite data for monitoring Air Quality in Norway using downscaling techniques” (Sat4AQN) project was to evaluate the potential of spatially downscaling satellite data using a high-resolution Chemical Transport Model (CTM) to spatial scales that are more relevant for monitoring air quality in urban areas and regional background sites in Norway. For this demonstration project, we focused on satellite aerosol optical density (AOD) and particulate matter (PM) estimates.

NORWEGIAN TITLE

Mot bedre utnyttelse av satellittdata for overvåkning av luftkvalitet i Norge ved hjelp av nedskaleringsteknikker (SAT4AQN)

KEYWORDS

Remote sensing	Downscaling	Air Quality	Aerosol optical depth / Particulate matter

ABSTRACT (in Norwegian)

Hovedmålet for prosjektet "Mot bedre utnyttelse av satellittdata for overvåking av luftkvalitet i Norge ved hjelp av nedskaleringsteknikker" (Sat4AQN) var å evaluere potensialet for romlig nedskalering av eksisterende satellittprodukter med støtte fra en høyoppløselig kjemisk transportmodell (CTM) til romlige skalaer som er mer relevante for å overvåke luftkvaliteten i urbane områder og regionale bakgrunnssteder i Norge. For dette demonstrasjonsprosjektet fokuserte vi på satellitt-aerosol-optisk tykkelse (AOD) og svevestøv (PM) estimater.

PUBLICATION TYPE: Digital document (pdf)	COVER PICTURE: Source: NILU

Towards better exploitation of Satellite data for monitoring Air Quality in Norway using downscaling techniques (SAT4AQN) Final project report

Kerstin Stebel, Philipp Schneider, Arve Kylling, and Tove Svendby

NILU - Norwegian Institute for Air Research

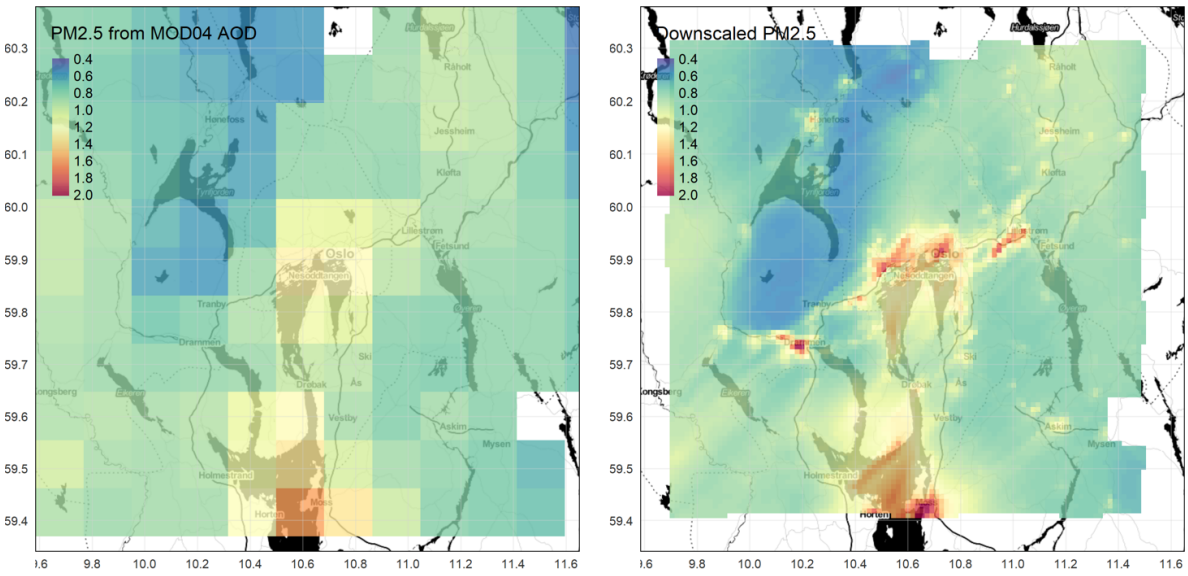

Figure on frontpage: Left panel: 10 km by 10 km surface $PM_{2.5}$ over Oslo for 28 May 2014 12 UTC derived from MODIS MOD04 AOD using simple model–based AOD to $PM_{2.5}$ ratio. Right panel: Downscaled 1 km by 1 km surface $PM_{2.5}$ over Oslo for 28 May 2014 12 UTC. Spatial proxy information from WRF–EMEP run.

Contents

List of Figures

List of Tables

1 Introduction

The main goal for the "*Towards better exploitation of Satellite data for monitoring Air Quality in Norway using downscaling techniques*" (Sat4AQN) project was to evaluate the potential of spatially downscaling existing satellite products with the support of a high-resolution Chemical Transport Model (CTM) to spatial scales that are more relevant for monitoring air quality in urban areas and regional background sites in Norway.

During the last years, the spatial resolution of satellite data has increased. A comparison of recent sensor spatial resolution is given in Fig. 1. GOME, which was launched on-board ERS-2, in April 1995 had a horizontal resolution of between 40 x 40 km^2 to 40 x 320 km^2. The TROPOMI instrument on the Sentinel-5P platform, launched on October 13, 2017, has a significantly smaller pixel size of 3.5 x 7 km^2, a larger swath-width (2600 km) and daily global coverage. While this is a major step forward for atmospheric composition monitoring, it is still not sufficent to capture features on local, i.e. city scales. Therefore, this project looked into the possibility to downscale the satellite data to gain spatial information at sub-pixel level.

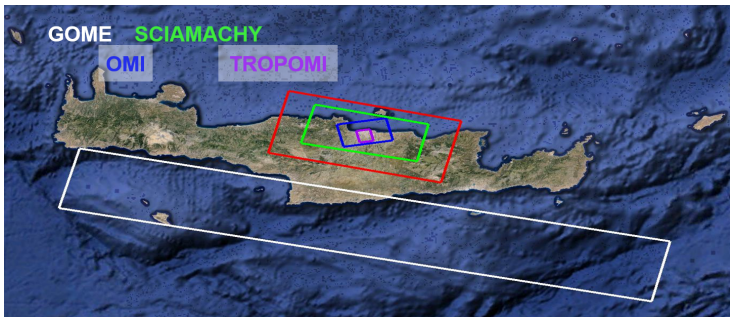

Figure 1 – Satellite sensor spatial resolution [Courtesy ESA].

More specifically, the aim of the Sat4AQN project was to demonstrate the improvements in spatial detail and accuracy that can be achieved with respect to air quality monitoring by downscaling current satellite data products using high-resolution information obtained from the EMEP-WRF model for Oslo city and the area around the Birkenes observatory (N 58°23′, E 08°15′, 190 m a.s.l) in Agder county, which is a National monitoring site for greenhouse gases and aerosols.

In general, the air quality in Norway has improved in recent years. Nevertheless, nitrogen dioxide (NO_2) and particulate matter (PM) continue to be of major concern in the urban areas, especially during winter. For this demonstration project, we focused on satellite aerosol optical density (AOD) and PM estimates. The reason for this is that ground-based AOD and PM observations, as well as low and high spatial resolution satellite AOD data, are available, which can be used to directly compare the performance of the downscaling.

The general structure of the Sat4AQN demonstration project is outlined in Fig. 2. The project was organized in eight tasks, which are described in more detail in the following.

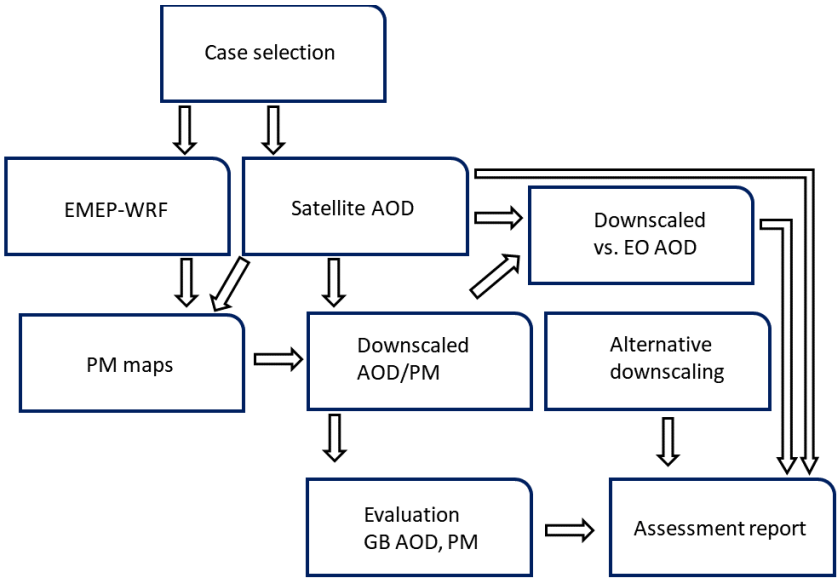

Figure 2 – General structure of the Sat4AQN demonstration project. Abbreviations: earth observation (EO), ground based (GB), particulate matter (PM), aerosol optical density (AOD), European Monitoring and Evaluation Programme (EMEP), Weather Research Forecast (WRF)

2 Task 1: Choice of episodes - time period

The time period for Sat4AQN was chosen based on the availability of ground-based AOD and PM data. AOD measurements started at Birkenes Observatory in spring 2009, using an automatic solar and sky radiometer (CIMEL type CE-318, instrument # 513). The AERONET direct sun algorithm (for details: http://aeronet.gsfc.nasa.gov) outputs quality assured and cloud-free level 2 data.

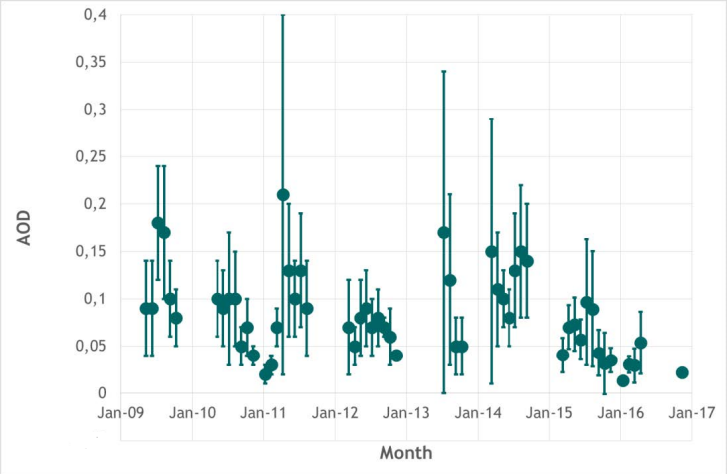

Figure 3 – 2009 - 2016 time series of aerosol optical depth (AOD) at 500 nm wavelength in the atmospheric column above Birkenes. Mean values and standard deviations are given [adapted from (Myhre et al., 2017)].

AOD for 500 nm from the start of measurements in 2009 to 2016, and AOD and $PM_{2.5}$ concentrations

for 2014 are shown in Fig. 3 and Fig. 4, respectively. For 2014, AOD measurements are available between March and September. Gravimetric measurements of particle mass concentration are only available as weekly averages that do not fit this study. Therefore, we use hourly data ($PM_{2.5}$) from an optical particle counter (OPC, this must be adapted to more accurate gravimetric data). We choose to start with the period from May to September 2014, where AOD and PM values were relatively high.

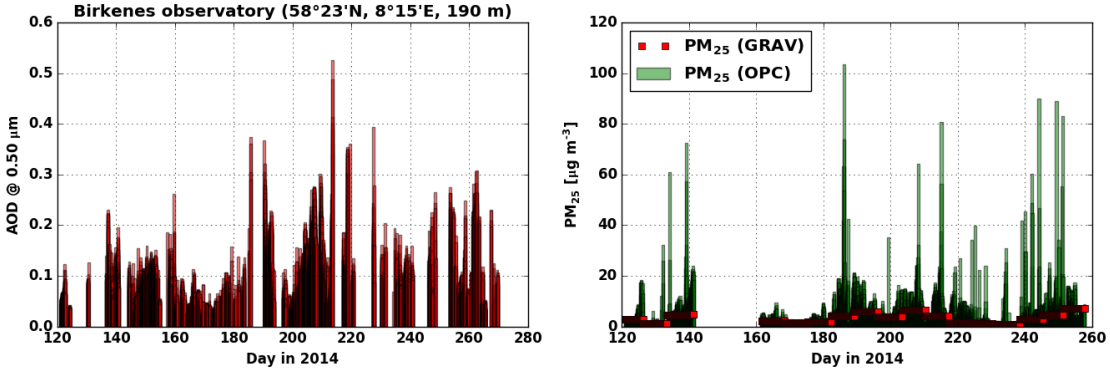

Figure 4 – AOD @ 500 nm (left panel) and $PM_{2.5}$ (right panel) between May and September 2014 measured at the Birkenes observatory.

For Oslo, the episode selection was basically based on a time series from the last seven years of $PM_{2.5}$ data and cloud information from Blindern Meteorological Station (Fig. 5). The data show that $PM_{2.5}$ episodes with major contamination in Oslo occur mainly in the winter months (especially December, January and February). This is because the main source of $PM_{2.5}$ in Oslo is wood burning from households. Since satellite data for AOD in these months is generally unavailable due to short days of low sun that provide few valid satellite observations, it was chosen to use the same test period for Oslo as for Birkenes station (summer 2014).

3 Task 2: WRF–EMEP model runs

The aim of project was to improve spatial details and accuracy in aerosol optical depth (AOD) and particulate matter (PM) by downscaling satellite data products using high-resolution information obtained from the WRF-EMEP model system. The objective of Task 2 was to perform the appropriate model simulations. Two locations were selected: the Oslo city and the area around the Birkenes observatory in Aust-Agder. At Birkenes, advanced aerosol and AOD measurements are available for validation.

For the WRF–EMEP model system the meteorological data are generated with the Weather Research and Forecast (WRF) model (Skamarock and Klemp, 2008). This is a flexible, state-of-the-art atmospheric model suitable for use in a broad range of applications across scales ranging from meters to thousands of kilometres. The WRF output is used as a meteorological driver for the EMEP model (Simpson et al., 2012), where dispersion and air chemistry can be solved.

A significant fraction of pollutants measured in Norway are transported from regions outside Europe, thus long-rang transport of air masses need be included in the model to simulate realistic aerosol concentrations. For the time period selected in Task 1, i.e. May – September 2014, nested model runs were performed.

The WRF and EMEP models were run on four nested grids: A mother domain of 50 km resolution covering Europe, a second domain covering Southern and Eastern Norway with a resolution of 10 km, and two inner domains with a resolution of 1 km covering Birkenes and Oslo, respectively. The inner domains of 1 km spatial resolution covered a region of 100 km x 100 km. Concentration of pollutants from the outer domain served as boundaries for the inner domains. The emission inventory for the outer domain was from the official EMEP 2014 country total emissions (EMEP Status Report 1/2016; http://emep.int/publ/reports/2016/EMEP_Status_Report_1_2016.pdf). Fine resolution emission data for Oslo and Birkenes were based on results from the NordicWelfAir project (http://projects.au.dk/nordicwelfair/). Tools were developed to prepare gridded emission files of eight compounds (SO_x, NO_x, NMVOC, CO, NH_3, $PM_{2.5}$, PM_{10}), where annual totals of each compound were distributed in 10 appropriate emission sectors. As an example, Fig. 6 shows annual emissions of NO_x, sector 7 (road emission) in the Oslo and Birkenes model domains.

The WRF-EMEP model system provided hourly output for a variety of pollutants. For Sat4AQN AOD values as well as model based $PM_{2.5}$ and AOD were selected for the desired period and domains shown in Fig. 6. The aerosol data served as input for the downscaling activity described in Task 5.

4 Task 3: Selection of satellite AOD products

In Table 1 an overview is provided of satellite data products that were considered to be used for downscaling and evaluation of the downscaled products.

The episode choosen was May – September 2014. SENTINEL-3 Sea and Land Surface Temperature

[1]MODIS MxD04_3 description is found at `https://ladsweb.modaps.eosdis.nasa.gov/api/v1/productPage/product=MOD04_3K`.

[2]MODIS MCD19A2 description is found at `https://lpdaac.usgs.gov/dataset_discovery/modis/modis_products_table/mcd19a2_v006`.

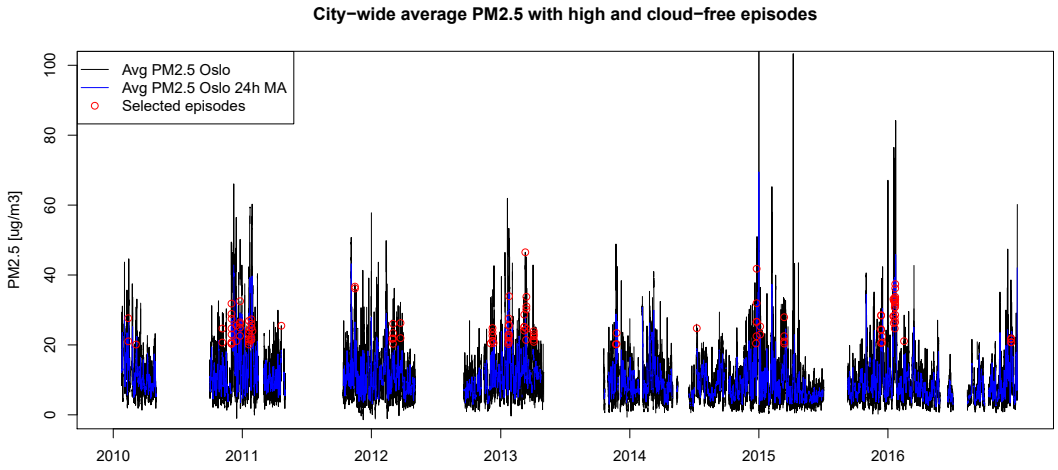

Figure 5 – Averaged hourly $PM_{2.5}$ concentration from all air quality monitoring stations in Oslo (black line). The blue line shows a 24-hour moving average. Red markers indicate hours where both the absolute concentration and the moving average were above a certain limit, and the cloud in Oslo measured at Blindern meteorological station was less than 2/8.

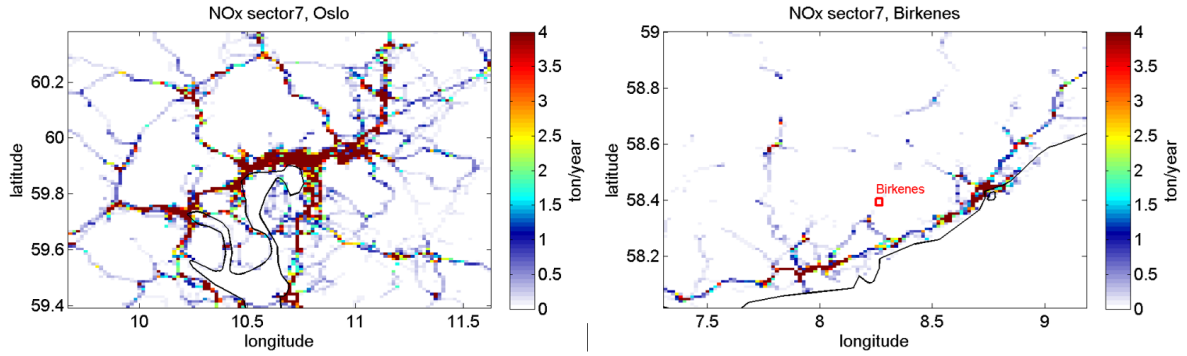

Figure 6 – Annual gridded emission of NOx from roads, sector 7, in Oslo (left) and the Birkenes area (right). Emissions are in ton/year.

Table 1 – Overview over satellite AOD data, their spatial scale and data access.

Sensor	Algorithm/data product	Spatial Resolution	Data access	Comments
SLSTR/OLCI	Level2_SYN_	OLCI PR ∼300 m SLSTR: 0.5-1 km	NRT Eumetsast	First launch 16.02.2016.
AATSR	Univ Swansea v4.2, ORAC v 3.02 FMI, ADV v2.3 or higher	10×10 km^2	ESA, Aerosol_CCI	Data until 02.2012.
VIIRS	Environmental Data Record (EDR)	6×6 km^2	NOAA CLASS	Overpass time differs from MODIS
VIIRS	Intermediate Products (IP)	0.75×0.75 km^2	NOAA CLASS	Overpass time differs from MODIS
MODIS Terra (x =O) MODIS Aqua (x = Y) Collection 6 (C6)	Deep Blue (DB). Dark Target (DT), Merged product, MxD04_L2	10×10 km^2 at nadir	NASA public	Used for downscaling
MODIS	MxD04_3K[1]	3×3 km^2	NASA public	Available for evaluation
MODIS	MCD19A2[2]	1×1 km^2	LP DAAC	Available for evaluation

Radiometer/Ocean and Land Colour Instrument (SLSTR/OLCI) and ENVISAT Advanced Along-Track Scanning Radiometer (AASTR) data are not available for 2014. Data from Visible Infrared Imaging Radiometer Suite (VIIRS) aboard the joint NASA/NOAA Suomi National Polar-orbiting Partnership (Suomi-NPP) are available, however, the VIIRS overpass time may differ from the Moderate Resolution Imaging Spectroradiometer (MODIS) by up to 45-90 minutes. During this time the aerosol may have moved thus possibly distorting comparisons between products from the two platforms. Hence, we used MODIS 10×10 km^2 AOD for downscaling, for which data products with higher spatial resolution (MxD04_3K at 3×3 km^2 and MCD19A2 at 1×1 km^2) are available, which can be used for evaluation.

5 Task 4: Derive $PM_{2.5}$ maps from satellite AOD

5.1 Processing

The main focus of Task 4 was to generate surface-level particulate matter concentration maps of particulate matter with particle diameter less than 2.5 μm ($PM_{2.5}$) from the selected AOD satellite product. We used the methodology first suggested by van Donkelaar et al. (2010), which calculates

a satellite-derived surface $PM_{2.5}$ estimate ($PM2.5_{sat}$) by multiplying the satellite-based AOD value with the fraction of model-derived $PM_{2.5}$ and model-derived AOD such that

$$PM2.5_{sat} = \frac{PM2.5_{mod}}{AOD_{mod}} \times AOD_{sat} \quad (1)$$

We used this approach to calculate satellite-derived surface $PM_{2.5}$ for our study domains of Oslo and Birkenes for all usable satellite overpasses during the study period of 1 May 2014 through 30 September 2014. The satellite product we used for this purpose was the MODIS MOD04 AOD product. We acquired and processed a total number of 934 MOD04 files. These files were converted from HDF4 to GeoTIFF using custom-written code and further processed to flag all pixels as invalid that did not have retrieval QA flags of at least 2 (good) or 3 (very good). In addition, the processing step included cropping the AOD data to the area of our two study site domains and reprojecting them to UTM32N projection with WGS84 datum. It should be noted here that a large fraction of the collected satellite datasets was too cloudy or suffered from other retrieval issues, such that in the end only a relatively small number of a few dozen scenes was considered useful for further processing.

5.2 Results

For the model data provided by the WRF–EMEP model, code was developed to read and re-project the dataset. Then the model-based AOD to $PM_{2.5}$ ratio was calculated for all hours in the entire study period. The model information was further resampled in terms of spatial extent and spatial resolution to match the MODIS MOD04 AOD dataset. All tasks were carried out for both the Oslo and Birkenes domains. Subsequently routines were developed for matching the satellite overpasses and model dates/times and automatically selecting on the relevant match-ups. Fig. 7 shows an example of the MODIS-derived surface $PM_{2.5}$ product for a few selected (non-cloudy) overpasses for the greater Oslo region. Similarly Fig. 8 shows the same but for the Birkenes study site.

6 Task 5: Alternative downscaling methods

6.1 Previous work

"Downscaling refers to an increase in spatial resolution" (Atkinson, 2013). It is used for example to increase the spatial resolution of results from global climate models to allow local impact studies (Wilby and Wigley, 1997). In satellite remote sensing downscaling is the decrease in pixel size of remotely sensed images. The coarse resolution variable of interest is downscaled using other high resolution imagery of either the same quantity (but with poorer time resolution) or a connected quantity. An example is downscaling of coarse resolution soil moisture from microwave measurements using solar and thermal higher resolution images (Im et al., 2016). Another application is downscaling of Tropical Rainfall Measuring Mission (TRMM) precipitation data to allow local analysis (Park, 2013). Other usages include downscaling of land cover mapping, land surface temperature, impervious surface distribution, erythemal surface radiation, thermal imagery, evapotranspiration, and atmospheric trace gases (Kolios et al., 2013; VoPham et al., 2016; Wu and Murray, 2003; Zhang et al., 2012). Downscaling may give the impression of creating data out of nowhere. While this is indeed not so, one should keep in mind that "one strictly cannot obtain more information than one starts with" (Atkinson, 2013).

Most of the remote sensing relevant literature discusses remote sensing of the Earth surface. Atkinson (2013) provides a review of downscaling in remote sensing and the various techniques involved. Ha et al. (2013) reviewed numerous downscaling methods for remote sensing-based irrigation management. There has only been very limited literature on applying downscaling techniques to satellite remote sensing products of the atmosphere, despite their generally coarse spatial resolution. (Zhang et al., 2012) is one of the few examples, geostatistical downscaling of methane columns derived from SCIAMACHY data using spatial information from a vegetation index dataset.

To the best of our knowledge, downscaling techniques have to this date not been applied to satellite products of air quality.

6.2 Overview of downscaling methods

Area-to-point kriging with external drift (or regression area-to-point kriging) as described later in the document and used for SAT4AQN is by no means the only downscaling technique. In the literature a large amount of different techniques are described, of which we want to briefly highlight a few in the following paragraphs. Alternative downscaling methods include, among others, machine learning techniques such as artificial neural networks (ANN) and geostatistical methods using cokriging.

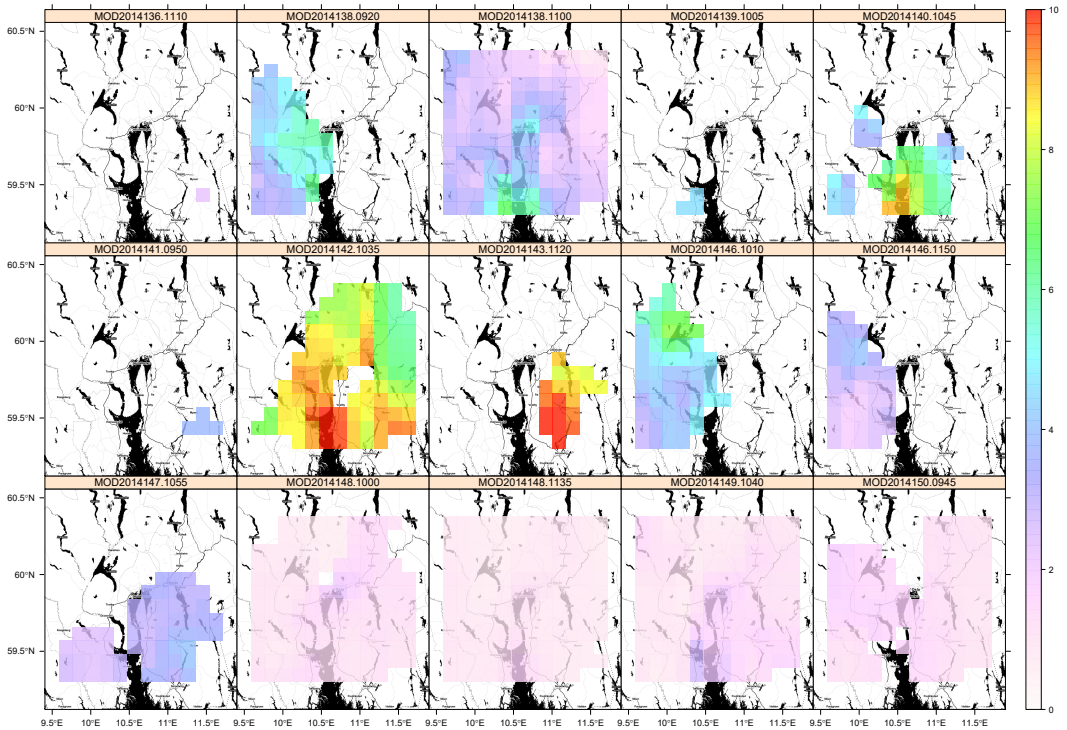

Figure 7 – Example of satellite-based $PM_{2.5}$ estimates (in units of $\mu g\ m^{-3}$) as derived from the MODIS MOD04 AOD product, here shown for a few overpasses for the area of Oslo and surroundings.

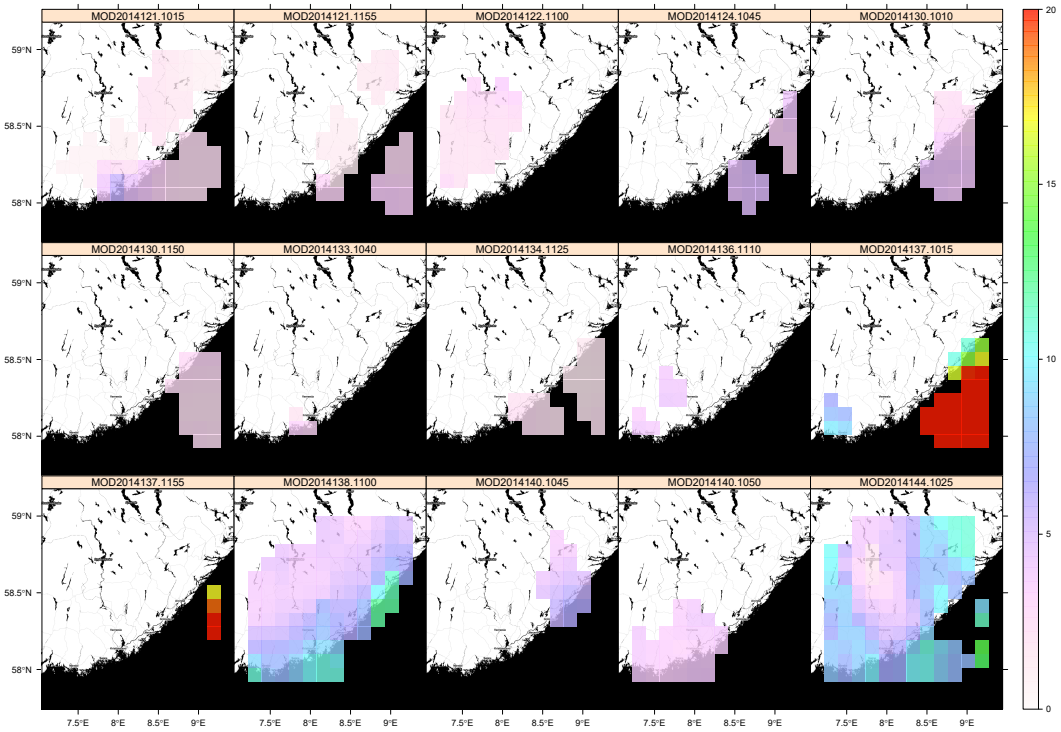

Figure 8 – Example of satellite-based $PM_{2.5}$ estimates (in units of $\mu g\ m^{-3}$) as derived from the MODIS MOD04 AOD product, here shown for a few overpasses for the area of Birkenes and surroundings.

6.2.1 Machine learning

Machine learning techniques may appear attractive as they allow computers to learn without being explicitly programmed. However, most of these techniques involve trial-and-error approaches to make the best selection of various model parameters. There are a number of machine learning methods. Below we discuss some of the methods that have been used for remote sensing applications. Note that this list is not complete.

Artificial neural networks (ANN) A brief history of artificial neural networks (ANN) and introduction is provided by Jensen et al. (2009). There are several classes of ANNs. One common method is the multilayer perceptron (MLP), used by for example Kolios et al. (2013) to downscale SEVIRI thermal images. The MLP has at least three layers of nodes: the input layer, one or more hidden layers, and one output layer. It is common to use one hidden layer. The ANN is trained through an iterative process, Fig. 9. As input Kolios et al. (2013) used combinations of SEVIRI pixel properties and the ANN provided output of thermal infrared radiation at MODIS spatial resolution. During the iterative training the training algorithm modified the weights of the ANN to minimize the difference between the output from ANN and the desired output (MODIS training data set).

Support vector machine (SVM) Support vector machines (SVMs) aim to establish optimal hyperplanes to linearly separate patterns in data. If patterns are not linearly separable, the original data may be mapped into a new space using kernel functions. SVMs are used for binary classifications and may be extended to a probabilistic setting through scaling. One of the strenghts

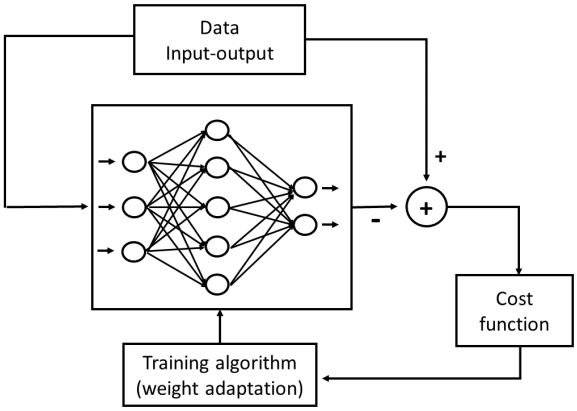

Figure 9 – Supervised training of an ANN with three layers: input, hidden and output (shown inside the box). The cost function takes as input the difference between the desired output and output from the ANN. The training algorithm modifies the weights of the ANN to find the optimal choice. Adopted from Kolios et al. (2013).

of SVMs is that it is not affected by local minima. The literature on SVMs is vast: a tutorial is provided by Burges (1998).

Relevance vector machine (RVM) Functionally relevance vector machine (RVM) has the same form as SVM. It was introduced by Tipping (2001). The main difference between RVM and SVM is that RVM uses far less kernel functions, furthermore the predictions from RVM are probabilistic while those from SVM are point estimates. A downside with RVM is that it is vulnerable to the risk of local minima.

Random forest The random forest method is based on a multitude of decision trees. For downscaling as discussed here, the target variable takes on continuous values and the decision trees are called regression trees. Random forest may be viewed as a way of averaging multiple decision trees. For selection of training samples, random forest gives the samples equal weights. Further information about the random forest method is found in Ho (1998) and Breiman (2001).

Boosted regression trees The boosted regression trees method is also based on decision trees. Contrary to the random forest method, during training it uses a weighting scheme that focus on the samples not well trained during the previous iteration. According to Im et al. (2016) this results in that "boosted regression trees sometimes have a tendency toward overfitting, regardless of the number of trees used".

Cubist The cubist technique is a regression tree system that produce rule-based predictive models. With each rule a multivariate regression is associated. This may be used to provides statistics so the relative importance of input parameters may be found. The Cubist technique has been used for several applications in remote sensing, see Im et al. (2016) and references therein.

6.2.2 Downscaling cokriging (DSCK)

To distinguish kriging and and cokriging we quote: "Kriging and cokriging are geostatistical techniques used for interpolation (mapping and contouring) purposes. Both methods are generalized forms of univariate and multivariate linear regression models, for estimation at a point, over an

area, or within a volume. They are linear-weighted averaging methods, similar to other interpolation methods; however, their weights depend not only on distance, but also on the direction and orientation of the neighboring data to the unsampled location"[1]. Furthermore; "Traditional regression methods only use data available at the target location and fail to use existing spatial correlations from secondary-data control points and the primary attribute to be estimated. Cokriging methods are used to take advantage of the covariance between two or more regionalized variables that are related, and are appropriate when the main attribute of interest is sparse, but related secondary information is abundant." Downscaling cokriging (DSCK) was first introduced in remote sensing by Pardo-Igúzquiza et al. (2006). Software for DSCK is described in Pardo-Iguzquiza et al. (2010).

6.2.3 Single normal equation simulation (SNESIM)

The methods described above utilizes spatial correlation of the fine scale attributes or an a priori spatial model in form of a variogram or similar. Such approaches have limitations to what spatial connections that can be accounted for. Specificially, spatial patterns can not be modeled with variograms. Boucher (2009a) used training images which included patterns that are also expected to be present in the actual image, to develop a method for generating pattern-accurate maps. In addition to downscaling coarse resolution images, the method also allows for the inclusion of other fine mapped features. An example is reproduced in Fig. 10, which shows the original Landsat image in the top. Boucher (2009b) used a training image from another location and then downscaled the upscaled original Landsat image (middle row, left). The downscaling was done by both excluding (bottom left image) and including (bottom right image) fine scale data of the water, road network and other impervious surfaces mapped in other ways (middle right image).

6.2.4 Spectral mixture analysis

Spectral mixture analysis is a physical rather than a statistical technique, which uses the entire spectrum of a pixel and a set of pure spectra of various surfaces (*endmembers*) to derive information bout the fractional abundance of each endmember within a given pixel. While it is thus not a downscaling methods per se, it can be used to provide constraints on the subpixel fractions. In addition, it does not require any additional information rather than the spectral information in the image and that endmember spectra. As an example, Wu and Murray (2003) estimated impervious surface distribution using spectral mixture analysis. Let R_b be the measured reflectance in band b for a pixel in the image. Then

$$R_b = \sum_{i=1}^{N} f_i R_{i,b} + e_b, \tag{2}$$

where f_i is the fraction of endmember i, $R_{i,b}$ is the reflectance of endmember i in band b and e_b is the unmodelled residual. The fraction f_i may be determined and provides information about the surface distribution.

6.2.5 Uncertainty estimates

Downscaled images may appear to have greated detail and contain more information than the starting coarse images. However, the initial information content in the coarse image put limits on what

[1] `http://petrowiki.org/Kriging_and_cokriging`

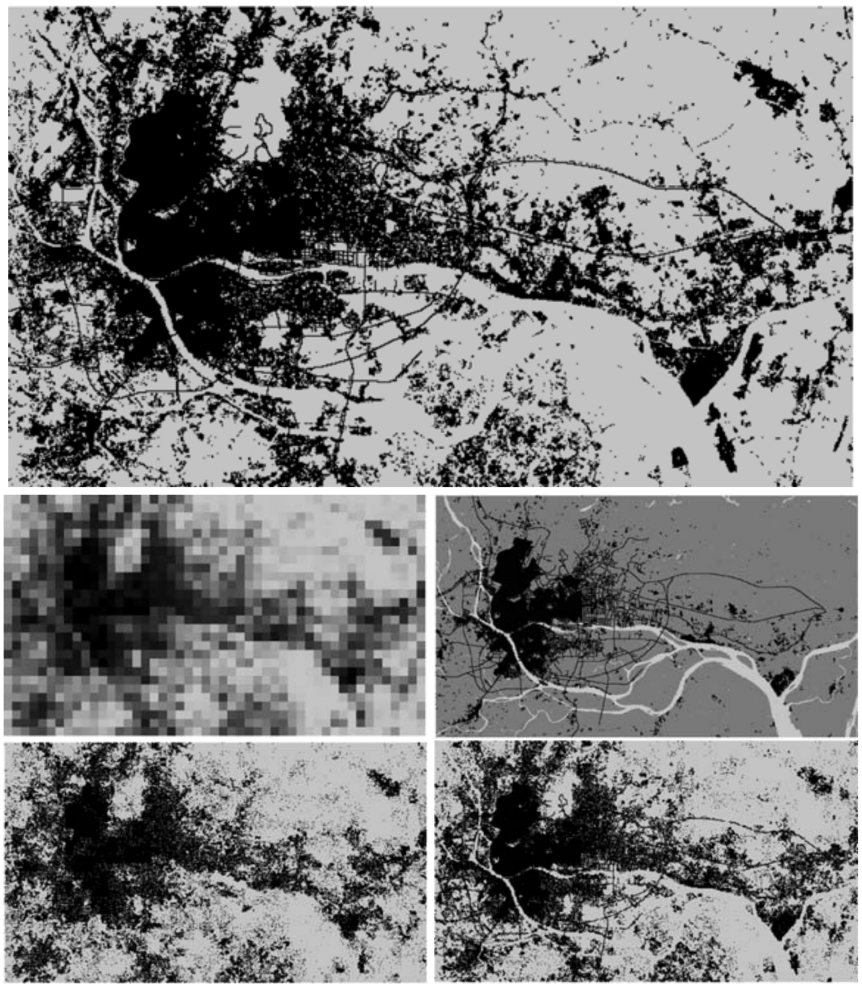

Figure 10 – Top row: Original Landsat image of impervious (black) and non-impervious (light grey) surfaces at 30 m resolution. Middle row: Upscaled Landsat image of the impervious class coarse fractions (left) and fine scale data of the water, road network and other impervious surfaces mapped in other ways (right).Bottom row: Downscaled image without fine scale data (left). Downscaled image including in fine scale data (right). Adopted from Boucher (2009b).

can be achieved in terms of downscaling. Hence, it is of great value to have some estimate of the local uncertainty in the downscaled image. This is seldom provided in the literature. In geostatistics one can use stochastic simulation to assess the spatial uncertainty. This may also be used for downscaling (Atkinson, 2013; Park, 2013).

6.3 Comparisons of downscaling methods

We are not aware of any study that systematically compares the multitude of downscaling methods. Below is mentioned some studies that compare two or more methods for specific applications.

The ANN, SVM and RVM methods have been compared by several authors. Srivastava et al. (2013) find that ANN performs better than SVM and RVM for several statistical parameters such as the coefficient of determination, R^2, the Root Mean Square Error (RMSE) and the percentage bias (%Bias),

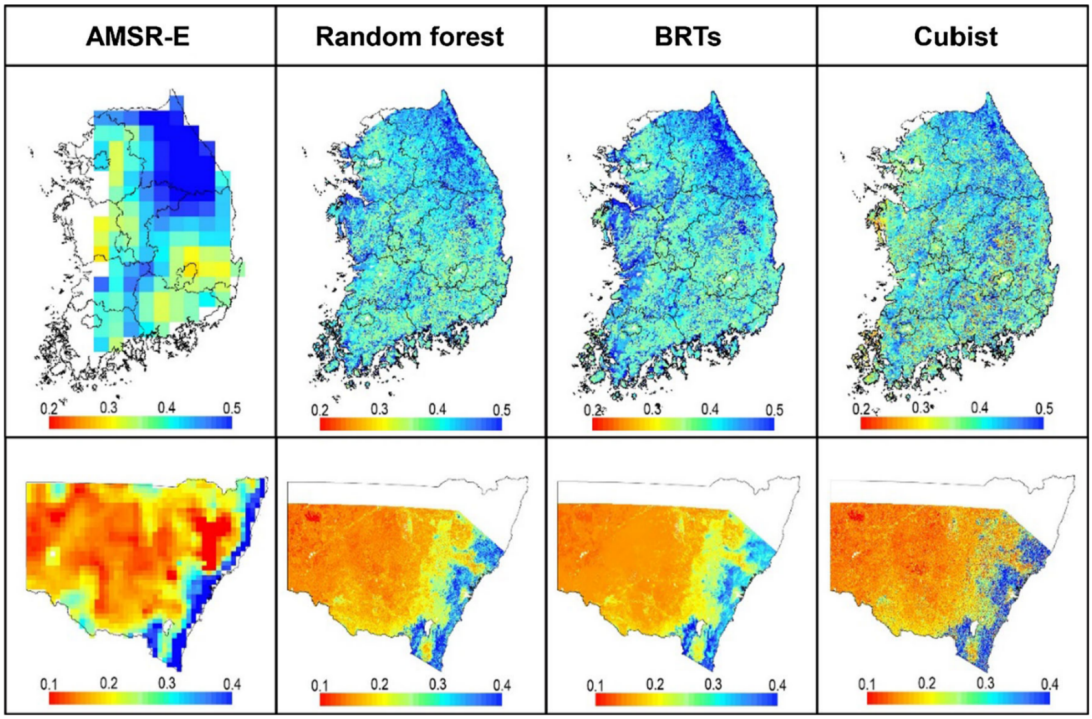

Figure 11 – Soil moisture derived from AMSR-E measurements and downscaled using the random forest, boosted regression trees (BRT) and cubist methods. The upper row shows South Korea for May 2007, while the bottom row is for New South Wales, Australia, January 2011. Adopted from Im et al. (2016).

when comparing down-scaled soil moisture. However, for downscaling of evapotranspiration and land surface temperatures, it is noted that several studies cited by Ha et al. (2013) found that the SVMs performed better than ANNs and also had a lower computational cost.

The random forest, boosted regression trees and cubist methods were compared for downscaling of soil moisture by Im et al. (2016). Examples of the original Advanced Microwave Scanning Radiometer on the Earth Observing System (AMSR-E) and downscaled data are given in Fig. 11. They found that the random forest method outperformed the two other methods. They also noted that "empirical machine learning approaches tend to reduce the dynamic range of a target variable".

Ke et al. (2016) compared the machine learning algorithms Support Vector Regression (SVR, a variation of SVM), Cubist and Random Forest. MODIS one kilometer evapotranspiration data were downscaled using Landsat-8 data. They found the Random Forest algorithm to produce the lowest error. However, the main control factor was the accuracy of the MODIS evapotranspiration data product.

Zhang et al. (2012) used ordinary kriging and ordinary cokriging to interpolate and downscale atmospheric methane column concentrations from the Scanning Imaging Absorption Spectrometer for Atmospheric Cartography (SCIAMACHY) instrument on the Environmental Satellite (ENVISAT). The original CH_4 had a spatial resolution of 50 km and was downscaled using the normalized difference vegetation index (NDVI) from MODIS at 5 km resolution. Based on various statistical estimators Zhang et al. (2012) found cokriging to perform better than kriging. To perform the study they used the software from Pardo-Iguzquiza et al. (2010).

7 Task 6: Downscaling of AOD and PM

7.1 Downscaling methodology

The downscaling methodology that was developed within the framework of the SAT4AQN project is based on geostatistics (Goovaerts, 1997; Isaaks and Srivastava, 1989; Wackernagel, 2003). More specifically we developed a variant of area-to-point kriging (Kyriakidis, 2004). In the following we describe the preliminary downscaling method that was selected for use within SAT4AQN. We first provide the theoretical basis of the algorithm and then describe the practical implementation.

7.1.1 Theory

Downscaling is essentially the prediction of unknown values at a fine spatial scale given known values at a coarse spatial scale. In geostatistical terms this is generally regarded as a change-of-support problem.

The downscaling methodology used here is, just like many other dowscaling techniques, essentially based on increasing the spatial resolution of a coarse source dataset (in our case satellite data of air quality) with the help of spatial proxy or auxiliary datasets that are available at a fine spatial resolution and that are to some extent correlated with the source dataset. As such the technique makes use of the assumption that the spatial patterns of the unknown fine-scale field of the source variable will be similar to the spatial patterns of the fine-scale proxy datasets.

More specifically, the technique that we use here follows that proposed by Park (2013), in that it combines a deterministic component (in this case linear regression against the high-resolution auxiliary variables) with a stochastic component (area-to-point kriging of the corresponding residuals), which is illustrated in Fig. 12. The field of the air quality related parameter (e.g. NO_2 column, surface NO_2 concentration, aerosol optical depth, surface $PM_{2.5}$) can be expressed at coarse scale as given by Park (2013) as

$$z(v_k) = a + \sum_{i=1}^{M} b_i \cdot y_i(v_k) + R(v_k) \tag{3}$$

where $z(v_k)$ are the the values of the variable in question at the coarse scale grid cell v_k (with $k = 1, \ldots, K$), i.e. for block support in geostatistical terminology, in which there are a total of K block supports. a and b_i are the regressions coefficients for $i = 1, \ldots, M$ auxiliary variables. $y_i(v_k)$ are the values of the fine resolution proxy datasets aggregated to the same coarse spatial scale as the data to be downscaled. $R(v_k)$ are the regression residuals at the scale of the coarse block support.

At the fine spatial scale, which is the target scale of the downscaling, the corresponding equation becomes

$$z^k(\mathbf{u}_n) = a + \sum_{i=1}^{M} b_i \cdot y_i^k(\mathbf{u}_n) + R^k(\mathbf{u}_n) \tag{4}$$

where $z^k(\mathbf{u}_n)$ denotes the predicted values of the variable in question at the grid cells given at fine spatial scale (target scale) within the k-th coarse grid cell. $y_i^k(\mathbf{u}_n)$ are the fine-scale predictor variables and $R^k(\mathbf{u}_n)$ are the residual values that cannot be accounted for by the deterministic linear relationship.

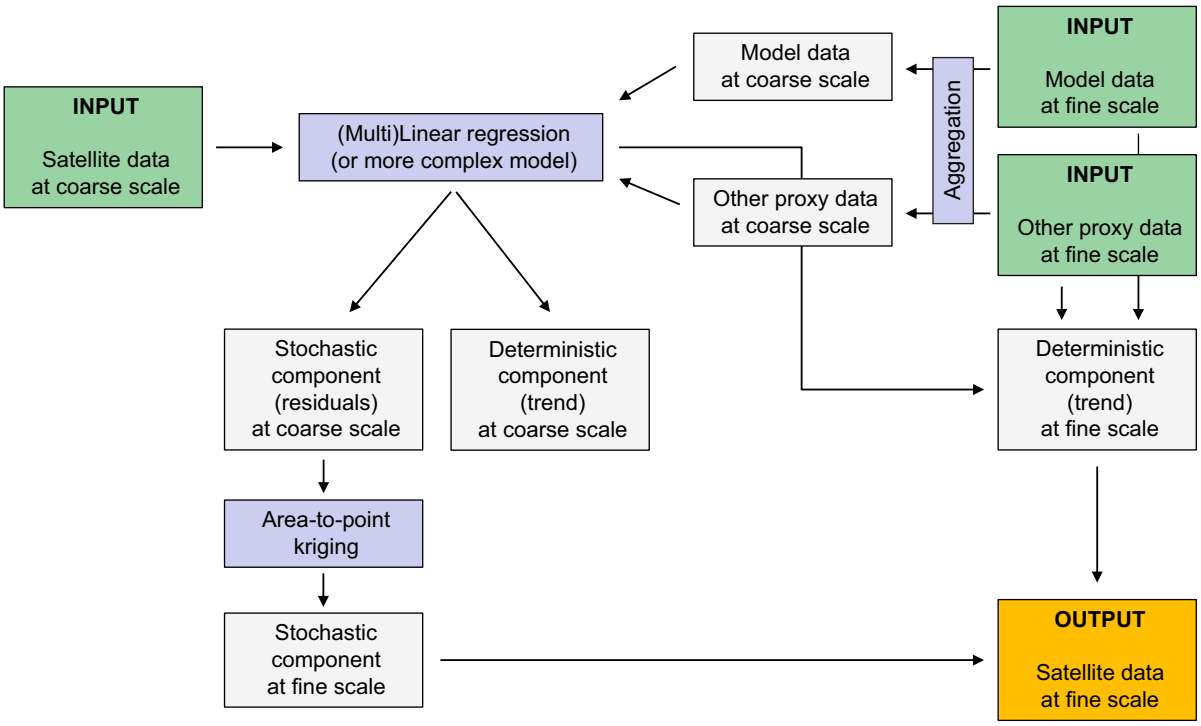

Figure 12 – The downscaling workflow developed for the SAT4AQN project.

The latter values are estimated at the fine spatial scale using area-to-point kriging using the coarse-resolution residuals of the deterministic component to predict the residuals at the fine spatial scale.

One of the crucial steps in doing this is to estimate the unknown point-support variogram from the known regularized variogram (i.e. the theoretical variogram fitted to the sample variogram of the coarse-resolution data). In other words, we are looking for the point-support variogram that, when regularized to the block support of the coarse-resolution datasets, results in the best fit to the actual observed sample variogram of the coarse-resolution dataset. This is generally carried out using an iterative process and can be implemented as a deconvolution process (Goovaerts, 2008) or an optimization technique (Skøien et al., 2014). Once the point-support variogram has been iteratively derived, it can then be used to solve the kriging system and to calculate the predicted values for the fine-scale support. The result is then a downscaled residual field of the variable in question, given for the fine spatial resolution. We call this the stochastic component.

After obtaining the stochastic component by carrying out the spatial downscaling of the residuals, the predictions of the deterministic component at the fine spatial scale and the downscaled residuals at the fine spatial scale are added, thus resulting in the final downscaled result.

A clear assumption of the described methodology is that there is a linear relationship between the variable in question and the auxiliary variables used as a proxy. If such a relationship is not existent, the deterministic component of the downscaling procedure does not add any value and the stochastic component alone drives the downscaling. The method then basically defaults to the technique proposed originally by Kyriakidis (2004), where no fine-scale proxy information is used but the only additional information aside from the coarse-resolution dataset comes from the point-level semivariogram which is estimated from the coarse-resolution data.

The advantage of separating the deterministic and the stochastic component in this downscaling

technique is that the deterministic component can be made arbitrarily complex. While we use here simple linear regression to establish the relationship between the variable to be dowscaled and the fine-scale spatial auxiliary variable, significantly more advanced non-linear statistical methods can be used to carry out this task. This could include machine learning approaches such as artifical neural networks, random forests, support vector machines, (boosted) regression trees, and many more. The practical implementation of such approaches could be accomplished with very little effort since only the deterministic component of the technique, which is currently based on linear regression, would have to be replaced with a different method. At the same time the rest of the algorithm is kept entirely the same. We suspect that the power of these more complex approaches will likely be most obvious when a larger number of auxiliary predictor variables is used.

7.1.2 Practical implementation

In order to carry out the downscaling for SAT4AQN, a new package called `dscaler` is being implemented in the R programming language (R Core Team, 2018). The package offers a simple and user-friendly interface by minimizing the number of required input parameters through providing sensible defaults. The package builts upon on a number of other R packages. This includes the `raster` package for providing spatial foundation classes for gridded data (Hijmans and van Etten, 2012) and the `sp` and `sf` (Pebesma, 2018) packages for providing spatial foundation classes for vector-based spatial information. Most importantly, the `rtop` package (Skøien et al., 2014) was used for estimating the point variogram from the coarse-resolution data and to solve the kriging systems for the area-to-point kriging of the residuals. The estimation of the point-support variogram is based on an iterative optimization procedure similar to the one proposed by Goovaerts (2008) and is described in detail in Skøien et al. (2006).

It should be noted that for reasons of computational efficiency the method uses a simplification in calculating in regularizing the point-support variograms. The iterative regularization requires the computation of point-to-point semivariogram values for all pairs of discretization points and is thus very expensive. Skøien et al. (2014) adapted the suggestion of Gottschalk et al. (2011) to simplify this calculation by using the the average distance between areas (as given by the average of all distances between all respective discretization point pairs) rather than integrating the covariance function for all distances, such that

$$d_{ij}^{*} = \frac{1}{|A_i|\,|A_j|} \int_{A_i} \int_{A_j} \left(\left| \overrightarrow{x_i} - \overrightarrow{x_j} \right| \right) d\overrightarrow{x_i} d\overrightarrow{x_j} \tag{5}$$

where d_{ij}^{*} represents the averaged distances between areas i and j with corresponding areas A_i and A_j, and where $\overrightarrow{x_i}$ and $\overrightarrow{x_j}$ are the position vectors between all discretizations points in the two areas. As such the regularized semivariance between two areas γ_{ij}^{*} can then be expressed as

$$\gamma_{ij}^{*} = \gamma_p(d_{ij}^{*}) - 0.5 \times \left[\gamma_p(d_{ii}^{*}) + \gamma_p(d_{jj}^{*}) \right] \tag{6}$$

as shown in Skøien et al. (2014).

The downscaling methodology described above is very entirely general and can be used regardless of the type of geophysical variables to be downscaled, as long as there is at least a minimal amount of correlation between the coarse-resolution and fine-resolution proxy dataset. Even if this is not the case, the method essentially defaults to ordinary area-to-point kriging as proposed by Kyriakidis (2004). It should be noted though that in such a case the spatial patterns of the downscaled results

will generally be quite smooth and will not exhibit the same level of accuracy that can be accomplished when a good fine-scale proxy dataset is being used. Nonetheless it will be significantly more accurate than traditional resampling techniques such as bilinear interpolation, cubic convolution, etc.

7.2 Downscaling results

7.2.1 Algorithm validation through simulated fields

The methodology was first tested on simulated fields. Such fields are simulated using unconditional sequential Gaussian simulation (Goovaerts, 1997). An example of such a field (with arbitrary units) is given in Fig. 13. Using simulated fields for testing the algorithm has the advantage that the fine-resolution truth is known and that the performance of the downscaling method can be evaluated accurately by comparing against the truth. Fig. 14 shows an example of downscaling such a simulated concentration field. The simulated field was assumed to be "true" state of the atmosphere. In practice, this truth is of course unknown and only serves as a reference here in this example. This field was then resampled to a coarser resolution (in this case by a factor of 10), which represents the coarse-resolution satellite-observed dataset. The goal of the algorithm is then to recover the true concentration field as good as possible using the coarse information from the satellite and a correlated auxiliary dataset. The performance of the downscaling procedure can be assessed by comparing the downscaled dataset with the original true dataset.

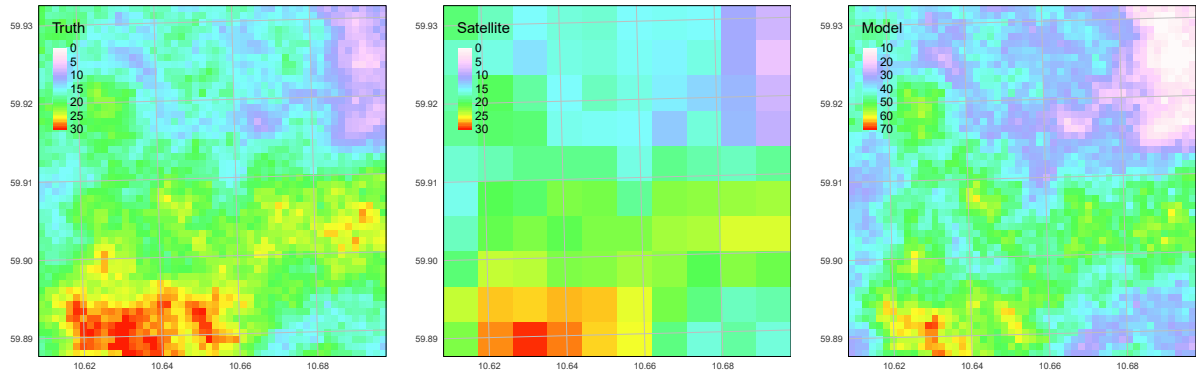

Figure 13 – Example of a simulated dataset created for comparing different downscaling methodologies. These datasets are produced using unconditional sequential Gaussian simulation (Goovaerts, 1997). The left panel shows the simulated true concentration field. The center panel shows a coarse-resolution version of the truth, which is assumed to be what the satellite sees. The right panel shows the output of a model (or any covariate to the truth) that can have entirely different values/units than the dataset to be downscaled but which is assumed to have spatial patterns that are at least somewhat correlated with the spatial patterns of the truth.

Figure 15 shows the output of various statistical downscaling methods with increasing level of complexity. The truth is given in the first panel as a reference. The SAT4AQN downscaling method is shown in the last panel. It can be seen that the spatial patterns of the SAT4AQN method most closely replicate the original spatial patterns of the truth dataset. Fig. 16 shows for each method the corresponding scatterplots comparing the true fine-scale value to the downscaled estimate of the same fine-scaled value. It can be observed that the best match between the two datasets is found for the SAT4AQN method, with an R^2 value of 0.98.

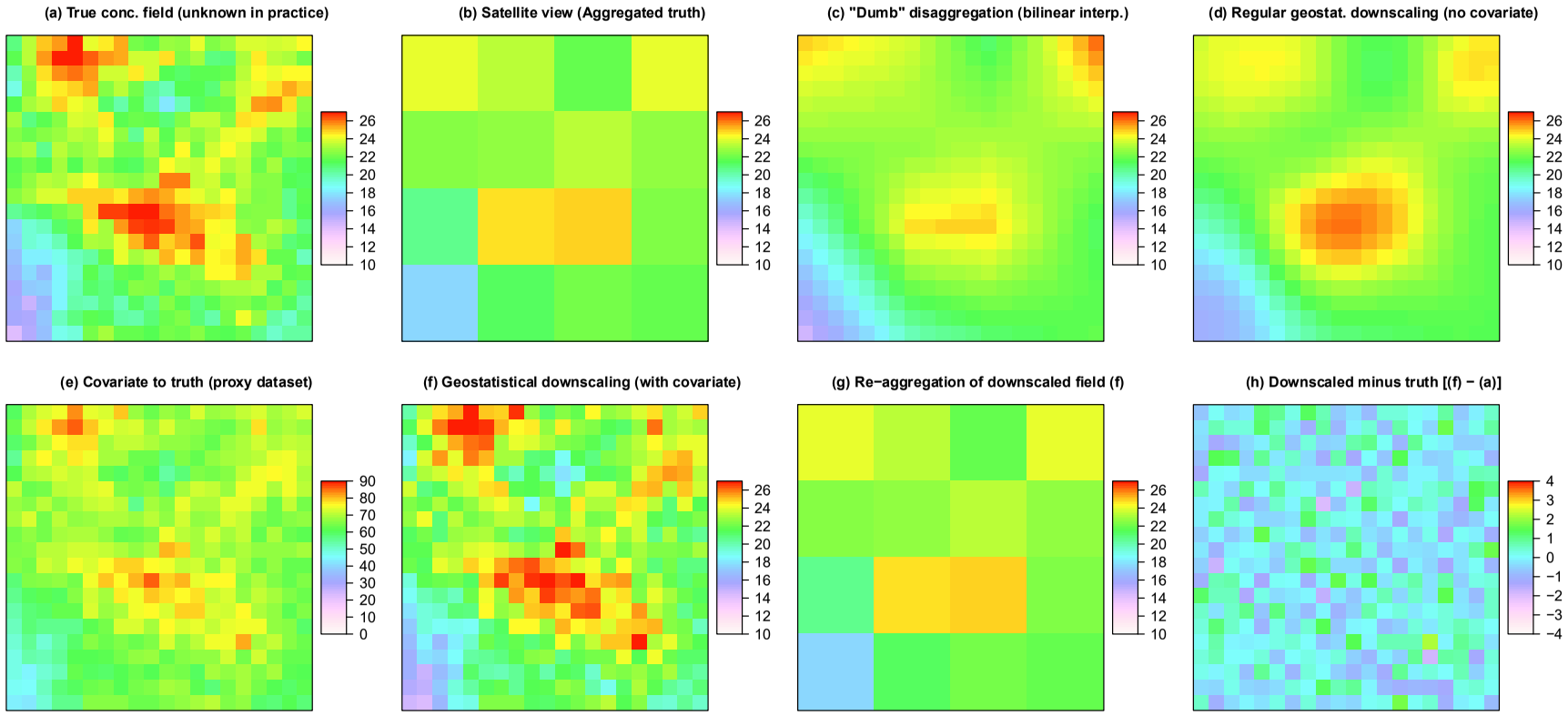

Figure 14 – Demonstration of the geostatistical downscaling methodology using a fictional simulated dataset. The method uses a simulated "true" concentration field (Panel a), which in practice is always unknown, to sample a coarse-resolution satellite dataset (Panel b). For reference, the result of '"downscaling"' this satellite dataset using simple bilinear interpolation is provided in Panel c). Panel d) shows the result of carrying out area-to-point kriging *without* a covariate variable, in which case the additional information used for the downscaling procedure comes solely from an estimated point variogram. However, the true power of the technique only shows when a covariate is used (Panel e). Note that this covariate has entirely different units than the variable to be dowscaled. Finally, Panel f) provides the result of area-to-point kriging of the satellite dataset *with* the covariate. Panel g) shows the re-aggregated downscaled to result, which indicates that the original spatial properties and values of the satellite dataset are preserved in the downscaling. Panel h) shows the difference between the simulated truth (Panel a) and the downscaled result (Panel f), which in this case is entirely random noise with a bias of zero.

Quantitatively, Table 2 shows the corresponding summary statistics for each method. The SAT4AQN method (area-to-point kriging with a covariate/trend) by far outperforms all the other methods by a significant margin. In particular the value of the root mean squared error (RMSE) decreases significantly for area-to-point kriging with a trend model from a value of 1.42 for simple bilinear interpolation to a value of 0.69. This is a more than two-fold increase in prediction accuracy and indicates that the SAT4AQN method by far provides the best performance of the tested downscaling algorithms. It should also be noted that the mean bias was found to be exactly equal to zero for the SAT4AQN method, indicating that despite using a proxy dataset with a possibly entirely different variable, the downscaling method does not introduce any bias to the original satellite dataset.

Table 2 – Summary statistics of a various downscaling methods for a simulated dataset. Marked in bold are the best values for the various metrics.

	Mean bias	SD	MAE	RMSE	Intercept	Slope	R^2
Bilinear interpolation (no covariate)	0.04	1.42	1.13	1.42	-0.73	1.04	0.91
Area-to-point kriging (no covariate)	-0.01	1.32	1.05	1.32	**-0.54**	**1.03**	0.93
Simple linear regression (with covariate)	-0.02	1.46	1.15	1.46	0.96	0.95	0.91
Robust linear regression (with covariate)	0.11	1.59	1.26	1.59	-3.11	1.17	0.91
Area-to-point kriging (with covariate)	**0.00**	**0.69**	**0.54**	**0.69**	0.95	0.95	**0.98**

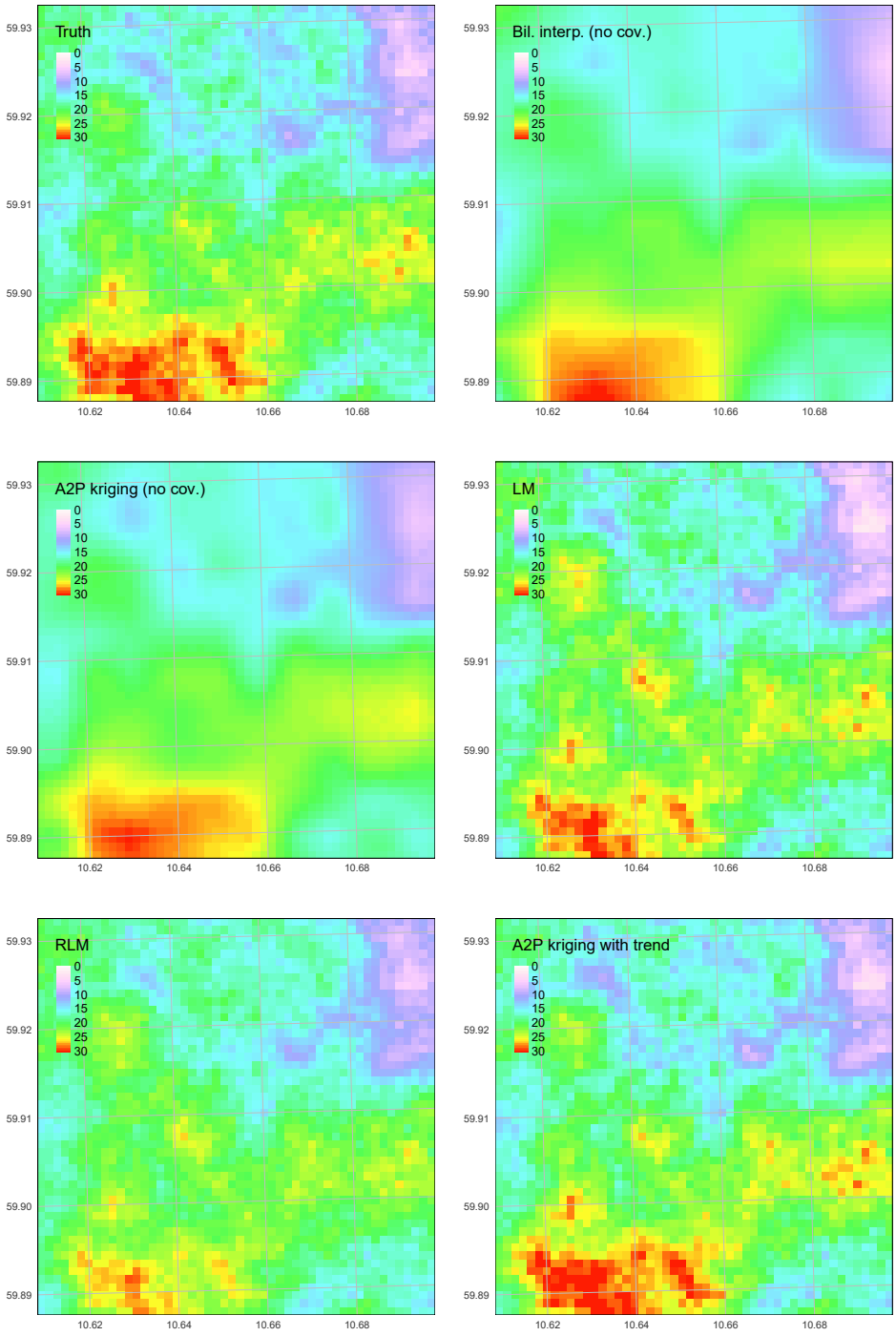

Figure 15 – Comparison of five different downscaling methods based on the dataset show in Figure 13 in order of increasing complexity. The top left panel shows the truth dataset for reference. The rest of the panels shows various downscaling methods, both with and without the use of a covariate/proxy dataset. Compare with Table 2 for a quantification of the accuracy of the downscaled results against the truth dataset. Note that the the method shows in the lower right panel (area-to-point kriging with a trend model) is best able to replicate the truth dataset. This is the method that has been chosen for the SAT4AQN project.

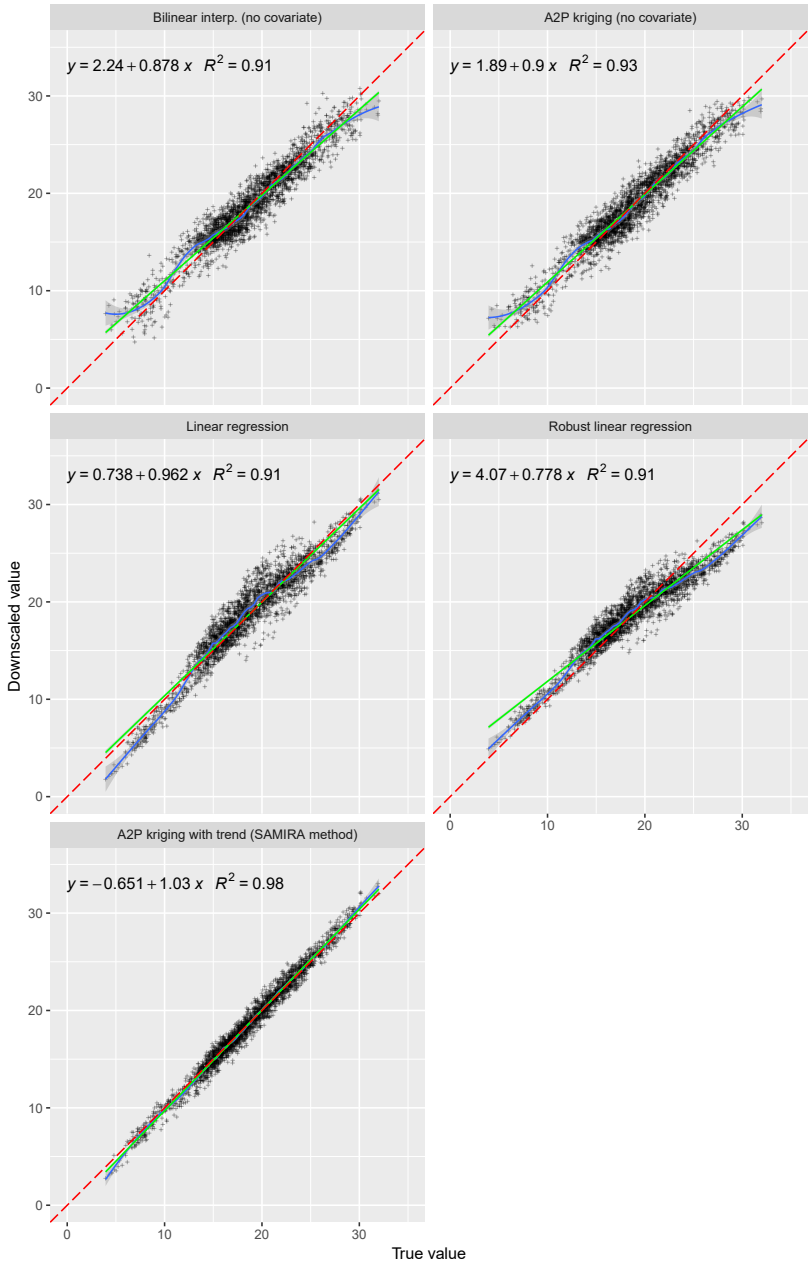

Figure 16 – Validation of the output of five different downscaling techniques against the simulated truth dataset. The dashed red line indicates the 1:1 line for reference. The blue line indicates a smooth loess fit to the data. The green line indicates a linear regression fit to the data, with the model coefficients and the R^2 value given in the top left corner of each panel.

7.2.2 Downscaling real-world satellite data

The downscaling methodology was applied to MODIS MOD04 AOD data and to $PM_{2.5}$ data derived from it. The EMEP model was used as a spatial proxy. It should be noted that the EMEP output of AOD was experimental and has not been thoroughly validated yet. AOD products over Norway tend to have substantial data gaps due to the often persistent cloud cover. The downscaling algorithm has been applied to all MOD04 overpasses within the study period (May 1 2014 through 30 September 2014) for which at least some valid retrievals were available. In the following we show some examples for both Oslo and Birkenes.

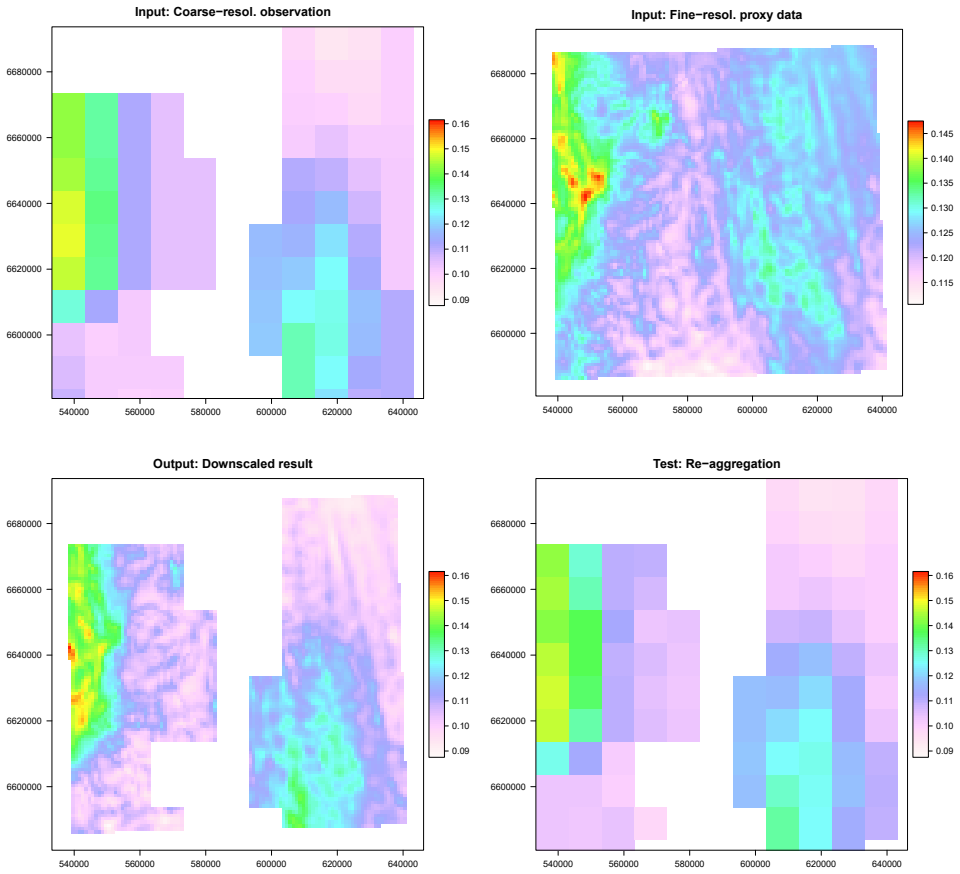

Figure 17 – Downscaling AOD for the greater Oslo region for 30 May 2014 at 09:45 UTC. The top left panel shows the coarse resolution satellite observations (ca. 10 km by 10 km MODIS MOD04 AOD data), the top right panel shows the corresponding AOD field provided by the EMEP model, the bottom left panel shows the results of downscaling the MOD04 product using the EMEP data as a spatial proxy, and the bottom right panel shows the result of re-aggregating the downscaled AOD field to the original satellite resolution.

Fig. 17 shows an example for downscaling AOD over the greater Oslo region. It can be observed that there is a reasonably good correspondence in terms of overall spatial patterns between the satellite-derived AOD product and the EMEP model output for AOD. The relatively high AOD values at the western edge of the study domain are present in both datasets. Further the moderately high AOD values in the southeast can also be observed in both the satellite and the model output. This correlation in overall spatial patterns is a good starting point for the downscaling algorithm.

The downscaled result looks quite reasonable in qualitative terms, but more thorough quantitative validation is needed. The Figure furthern shows how re-aggregating the downscaled results to the spatial resolution of the original satellite dataset results in nearly the same values, indicating that the method produces mostly unbiased results. The small discrepancies that can be seen between top left and the bottom right panels in Fig. 17 are likely due to aggregation artifacts from resampling and due to edge effects.

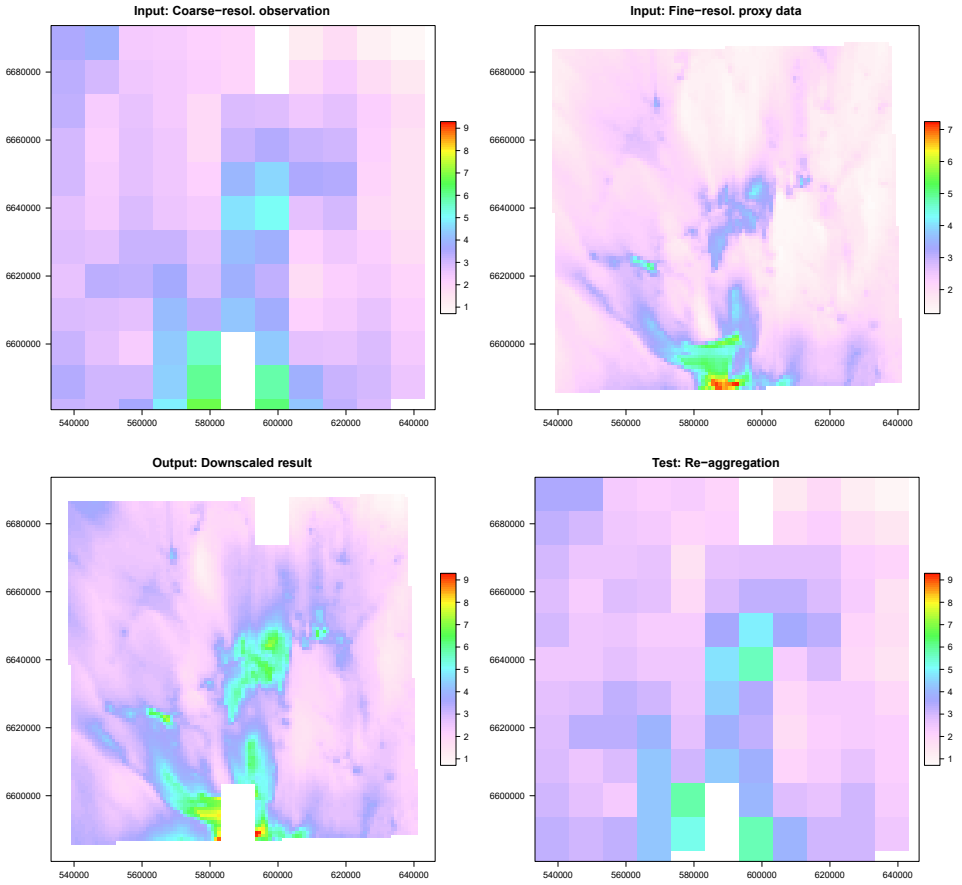

Figure 18 – Downscaling satellite-derived $PM_{2.5}$ for the greater Oslo region for 18 May 2014 at 11:00 UTC. The top left panel shows the coarse resolution satellite observations ($PM_{2.5}$ in μg m^{-3} derived from ca. 10 km by 10 km MODIS MOD04 AOD data), the top right panel shows the corresponding $PM_{2.5}$ field in μg m^{-3} provided by the EMEP model, the bottom left panel shows the result of downscaling the satellite product using the EMEP data as a spatial proxy (again in units of μg m^{-3}), and the bottom right panel shows the result of re-aggregating the downscaled AOD field to the original satellite resolution.

Fig. 18 shows an example of downscaling satellite-derived surface $PM_{2.5}$ fields. Once again, we see good correspondences in terms of spatial patterns between the satellite-derived dataset and the EMEP model ouput. In both dataset we can see a hotspot over the city area of Oslo (hotspots in the center of the domain) and some relatively high concentrations at the southern edge of the domain. Due to this correlation in terms of spatial patterns the output of the downscaling algorithms appears mostly reasonable and in fact it can provide additional details not observable in the original satellite-derived dataset, such as small but distinct hotspot to the southwest of the center that indiciates the area of the town Drammen.

Fig. 19 provides an example of downscaling AOD over the area of Birkenes in southern Norway. While

the correspondense between satellite data and EMEP model output is not as strong as in some of the previous plots, it is still possible to observe in both datasets a gradient in AOD values ranging from the relatively low values in the center of the study domain towards relatively high values located in the northeast corner. The downscaled AOD field thus provides overall qualitatively reasonable results, although not particular features of note are visible.

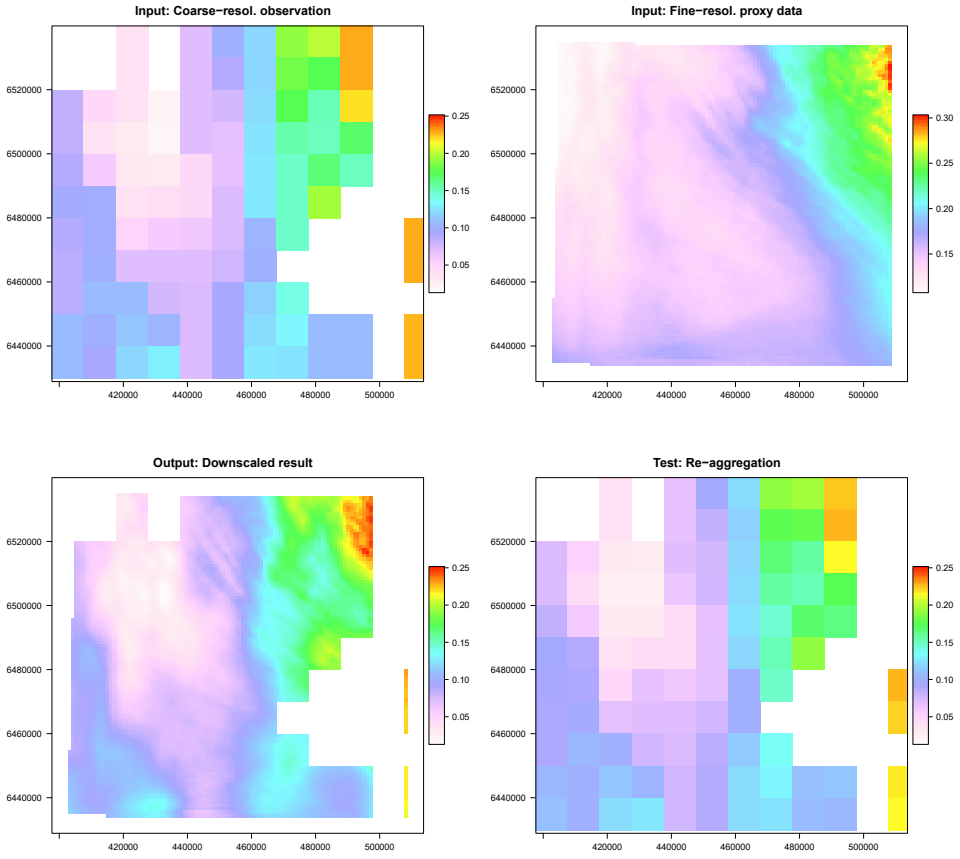

Figure 19 – Downscaling AOD for the greater Birkenes region for 24 May 2014 at 10:25 UTC. The top left panel shows the coarse resolution satellite observations (ca. 10 km by 10 km MODIS MOD04 AOD data), the top right panel shows the corresponding AOD field provided by the EMEP model, the bottom left panel shows the results of downscaling the MOD04 product using the EMEP data as a spatial proxy, and the bottom right panel shows the result of re-aggregating the downscaled AOD field to the original satellite resolution.

Finally, Figure 20 gives an example of downcaling $PM_{2.5}$ over the area of Birkenes. We can observe in both the satellite-derived $PM_{2.5}$ datasets as well as the EMEP model output that there is a imcreasing gradient from the northwest of the study domain towards the southeast. The downscaled results obviously also show this gradient but in addition the downscale map also contains four clear hotspots that it inherited from the model dataset. These hotspots represent the coastal towns of Kristiansand, Lillesand, Grimstad, and Arendal (from southwest to northeast) and are a good example of the type of value-added product that can be created by combining the coarse-resolution satellite dataset with fine-resolution model output. It should be noted again at this point that only the spatial patterns are inherited from the model dataset in this methodology and that the absolute values of the downscaled results are entirely driven by the satellite dataset.

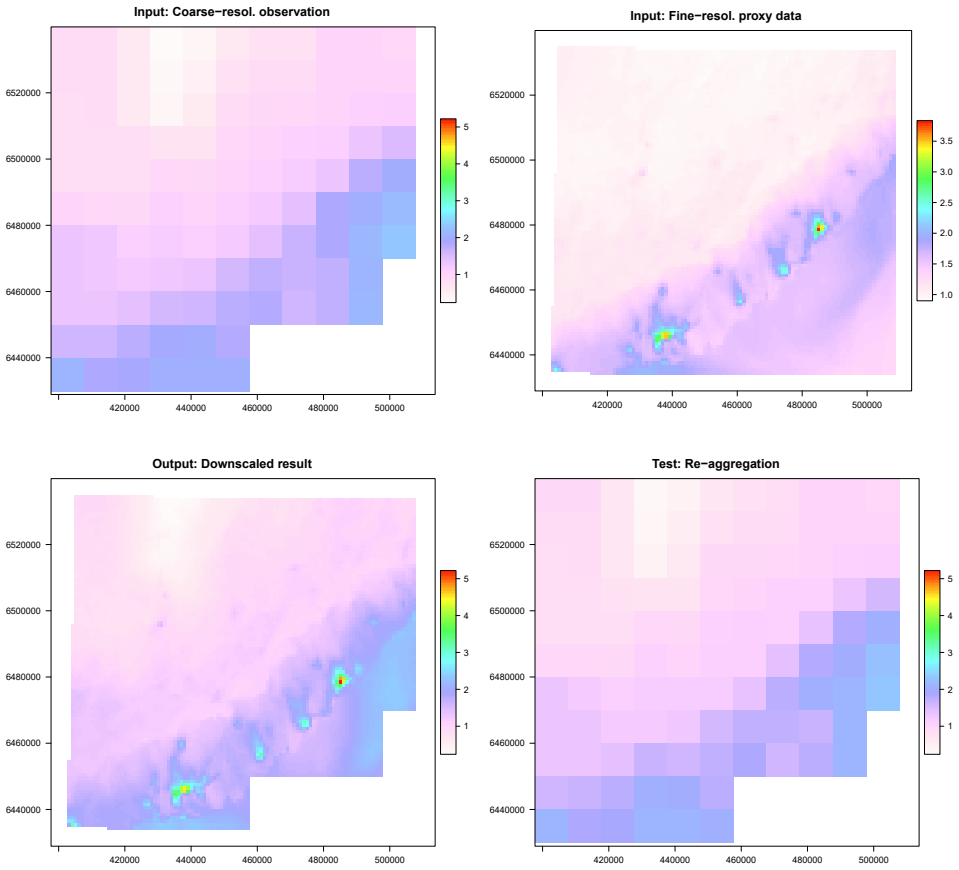

Figure 20 – Downscaling satellite-derived $PM_{2.5}$ for the greater Birkenes region for 29 May 2014 at 10:40 UTC. The top left panel shows the coarse resolution satellite observations ($PM_{2.5}$ in μg m^{-3} derived from ca. 10 km by 10 km MODIS MOD04 AOD data), the top right panel shows the corresponding $PM_{2.5}$ field in μg m^{-3} provided by the EMEP model, the bottom left panel shows the result of downscaling the satellite product using the EMEP data as a spatial proxy (again in units of μg m^{-3}), and the bottom right panel shows the result of re-aggregating the downscaled AOD field to the original satellite resolution.

8 Task 7: Evaluation with ground-based and satellite data

8.1 Ground-based evaluation

8.1.1 Birkenes

The satellite and downscaled data, i.e. AOD and $PM_{2.5}$ are compared with observations made at the Birkenes observatory in Aust Agder county. Fig. 21 shows the timeseries of MODIS AOD, downscaled AOD, satellite derived $PM_{2.5}$ and downscaled $PM_{2.5}$, as well as AERONET AOD and surface $PM_{2.5}$ measured during June – September 2014 at the Birkenes observatory (58°3'N, 8°E, 190 m a.s.l). For the AOD total column observations a good correlation is evident. The satellite derived $PM_{2.5}$ observations do not resemble the high values seen by the optical particle counter (OPC). Their absolute values are in the same oder of magnitude as the weekly gravimetric $PM_{2.5}$ observations.

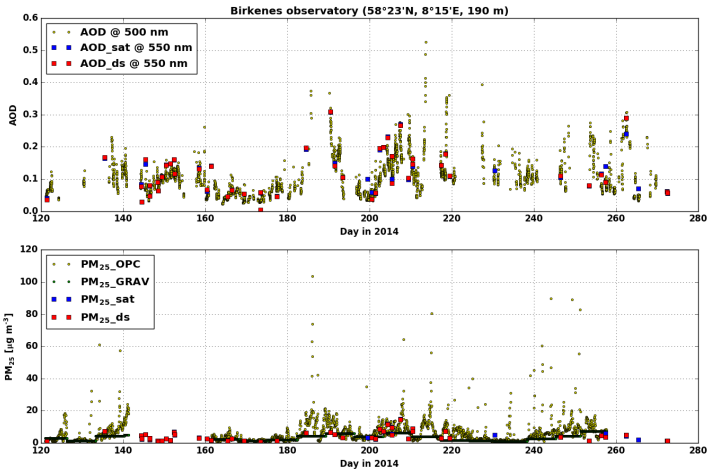

Figure 21 – Timeseries MODIS and downscaled AOD and $PM_{2.5}$ for June – September 2014 for the Birkenes observatory (58°3'N, 8°E, 190 m a.s.l). The upper panel shows MODIS AOD at 550 nm (red), downscalled AOD at 550 nm (blue) and AERONET AOD at 500 nm. The lower left panel shows satellite derived surface $PM_{2.5}$ (blue), downscaled satellite derived surface $PM_{2.5}$ (red), hourly $PM_{2.5}$ values from optical particle counter (OPC) (yellow) and weekly gravimetric $PM_{2.5}$ observations (yellow).

To look into the effect of the downscaling, in Fig. 22 the original and downscaled MODIS AOD and satellite derived $PM_{2.5}$ are shown, and the differences between MODIS AOD and downscaled AOD, and satellite $PM_{2.5}$ and downscaled $PM_{2.5}$ are given. For comparison, the AOD uncertainty given for the AERONET AOD @ 500 nm is 0.01. As the area around Birkenes is goverened by small gradients in total column aerosol distribution during the time period studied, the differences are small and only occasionally exceed the AERONET AOD uncertainty.

A comparison between MODIS and downscaled AOD and AERONET AOD, derived and downscaled $PM_{2.5}$ and OPC, gravimetric $PM_{2.5}$ data for June – September 2014 for Birkenes is shown in Fig. 23. We find a good correlation for AOD ($r^2 = 0.736$), which is marginally improved by downscaling ($r^2 = 0.738$). As expected, $PM_{2.5}$ derived via scaling shows a much lower correlation, but also in this case a marginally improvement is seen ($r^2 = 0.17$ for original data, $r^2 = 0.18$ for downscaled $PM_{2.5}$).

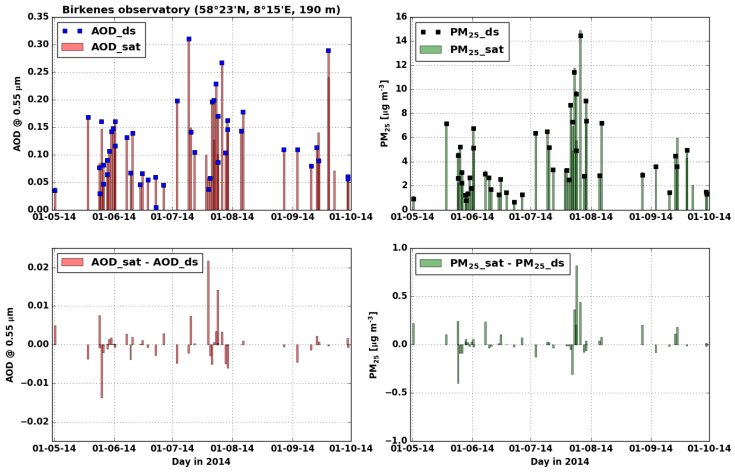

Figure 22 – Timeseries MODIS and downscaled AOD and $PM_{2.5}$ for June – September 2014 for the Birkenes observatory (58°3'N, 8°E, 190 m a.s.l). The upper left panel shows MODIS AOD (red) and downscalled AOD (blue). The upper right panel shows $PM_{2.5}$ derived from MODIS AOD (green) and downscalled $PM_{2.5}$ (blue). The lower panel show the effect of the downscaling on the original dataset, i.e. MODIS AOD - downscaled AOD (lower left panel) and satellite based $PM_{2.5}$– downscaled $PM_{2.5}$ (lower right panel)

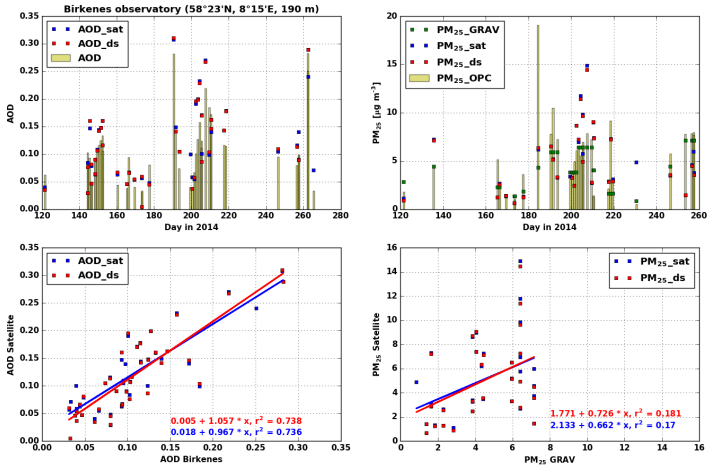

Figure 23 – Comparison between MODIS and downscaled AOD and AERONET AOD, derived and downscaled $PM_{2.5}$ and OPC, gravimetric $PM_{2.5}$ data for June – September 2014 for the Birkenes observatory. The upper left panel shows MODIS AOD (blue), downscalled AOD (red) in comparison with AERONET AOD (yellow). The upper right panel shows satellite derived surface $PM_{2.5}$ (blue), downscaled satellite derived surface $PM_{2.5}$ (red), hourly $PM_{2.5}$ values from optiocal particle counter (OPC) (yellow) and weekly gravimetric $PM_{2.5}$ observations (yellow). The lower left panel shows the correlation between MODIS AOD and AERONET AOD (blue), as well as the correlation between downscaled MODIS AOD and AERONET AOD (red).The lower right panel shows the correlation between satellite derived $PM_{2.5}$ and gravimetric $PM_{2.5}$ (blue), as well as the correlation between satellite derived $PM_{2.5}$ (blue) and gravimetric $PM_{2.5}$ (red).

8.1.2 Oslo

AOD is not measured in Olso. There are ten air quality stations within greater Oslo measuring $PM_{2.5}$, nevertheless nine stations are traffic sites, which are not representative on a scale of 1 km^2. Therefore we compare the satellite and downscaled $PM_{2.5}$ data to the data measured at the Sofienpark station, which is the only urban background site in Oslo (59.92295 N, 10.76573 E). For the evaluation of downscaled $PM_{2.5}$ at the Sofienpark station, in Tab. 3 the mean error, standard deviation, mean absolute errror and root mean square error (RMSE) for the orginal satellite derived $PM_{2.5}$ and the downscaled $PM_{2.5}$ data are shown. This comparison shows the improvement made by the downscaling, a small decrease in all values, e.g. the RMSE goes down from 9.3 (original $PM_{2.5}$) to 8.8 (downscaled $PM_{2.5}$).

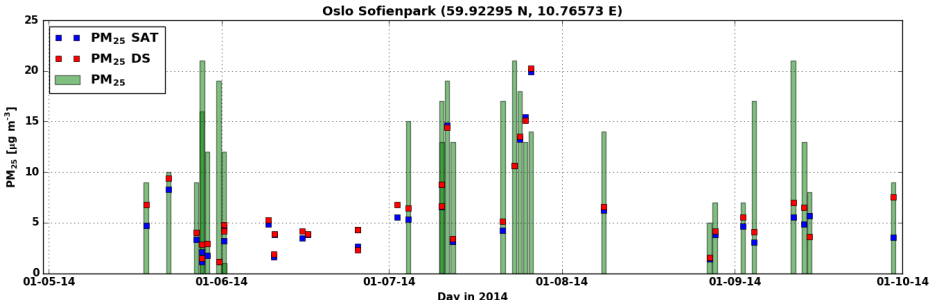

Figure 24 – Timeseries satellite derived $PM_{2.5}$ (blue), downscaled $PM_{2.5}$ (red) and hourly surface $PM_{2.5}$ (green) data for June – September 2014 measured at the Sofienpark station (59.92295 N, 10.76573 E) in Oslo.

Table 3 – Statistics for the comparison of satellite derived $PM_{2.5}$ and satellite derived downscaled $PM_{2.5}$ with surface $PM_{2.5}$ measured beween June – September 2014 at the Sofienpark station

Method	Mean error	Std. Dev.	Mean absolute error	RMSE
Original satellite product	7.1	6.1	8.0	9.3
Downscaled data	6.5	6.0	7.3	8.81

8.2 Satellite-based evaluation

In Tab. 1 an overview was provided of satellite data products that were considered to be used for evaluation of the downscaled products (see Task 3).

The downscaled AOD and MODIS AOD with spatial resolutions of 3×3 and 1×1 km^2 are shown in Fig. 25 for the AOD examples in section 7.2.2.

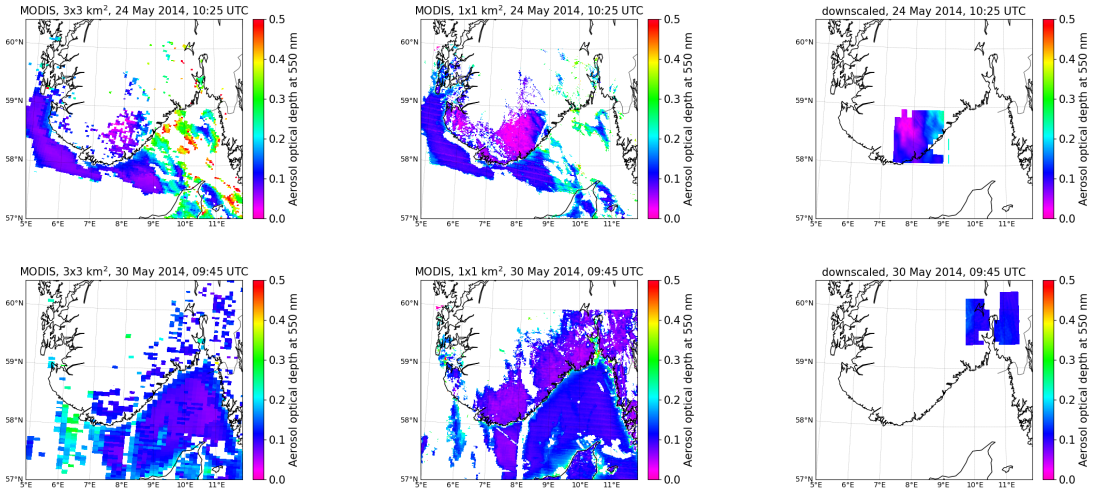

Figure 25 – Left and centre columns: AOD as retrieved from MODIS at 3×3 and 1×1 km^2 resolutions. Right column: AOD from downscaling. Top row is data from 24 May 2014, 10:25 UTC and bottom row is for 30 May 2014, 09:45 UTC.

For 24 May the downscaled AOD reproduces the spatial pattern seen in the MODIS AODs. The AOD distributions are also similar for the downscaled AOD and the MODIS AODs, see Fig. 26. For 30 May the downscaled AOD appears to be limited in range, missing the low AOD values, compared to the MODIS AODs. For both dates the downscaled AOD mean and median are within the values calculated from the MODIS AODs.

Pixels from the downscaled product may be directly compared with the MODIS AOD 3×3 km^2 values. The difference in AODs from overlapping downscaled and 3×3 km^2 pixels is shown in Fig. 27. The histograms show that on a regional basis, the downscaled AOD product reproduces the overall features of the MODIS AOD. However, for single locations differences may be pronounced, see plots in left column of Fig. 27.

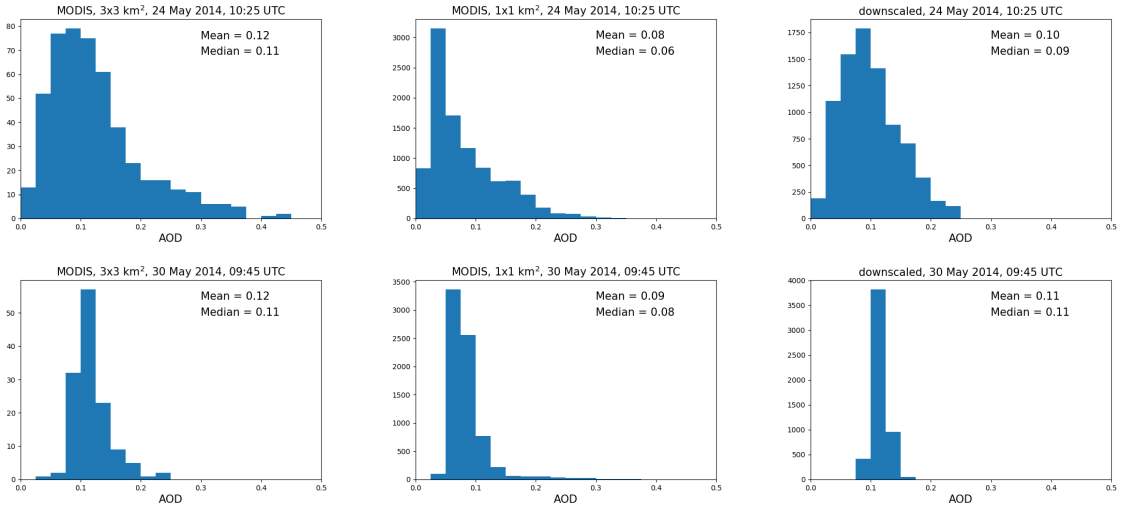

Figure 26 – Left and centre columns: Histograms of MODIS AOD for 3×3 and 1×1 km^2 resolutions. Right column: AOD histogram from downscaling. Top row is data from 24 May 2014, 10:25 UTC and bottom row is for 30 May 2014, 09:45 UTC. The mean and median values are included in each plot. Data included in the histograms were limited to those covered by the downscaled regions and latitudes $< 60°$.

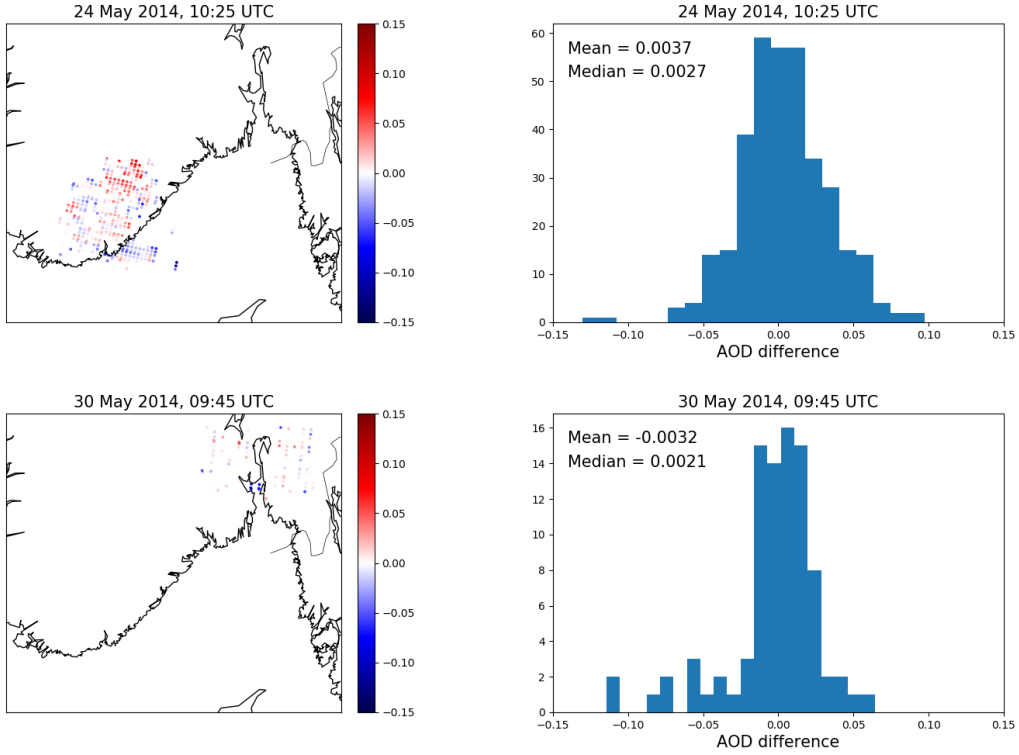

Figure 27 – Left column: Difference in AOD from overlapping downscaled and 3×3 km^2 resolution pixels. Right column: Histogram of difference in AOD. Top row is data from 24 May 2014, 10:25 UTC and bottom row is for 30 May 2014, 09:45 UTC.

9 Summary and Conclusions

It has been demonstrated that the downscaling technique developed as part of this project is capable of successfully increasing the spatial resolution of a coarse-resolution satellite product when a spatial proxy dataset at fine spatial resolution is available and the two datasets agree overall in terms of spatial patterns. Downscaling AOD is very challenging as the correlation between model output and satellite observations tends to be much weaker than for, say, nitrogen dioxide, where the emission sources are very well known and the short lifetime of the gas generally causes a rapid decreasing spatial gradient from the main emission hotspots. Nonetheless, we showed that for some cases, downscaling satellite-derived AOD and satellite-derived surface concentrations of $PM_{2.5}$ is feasible, but lead only to marginal improvements compared to the satellite dataset at coarser resolution.

Downscaling techniques are capable of successfully increasing the spatial resolution of a coarse-resolution satellite product and we foresee suitable applications. Downscaling techniques for pollutants that have a clearly defined source and a relatively short lifetimes in the atmosphere, such as nitrogen dioxide, should be further exploited. In such cases, quite good and robust results can be achieved as has been demonstrated as part of the ESA-funded SAMIRA project. Furthermore, downscaling of methane columns derived from TROPOMI using spatial information from a high resolution vegetation index dataset, e.g. from Sentinel-2, is an application worth exploiting in more detail.

As a final remark, it should also be noted that, the accuracy of the downscaled results can only be as good as the quality of its input datasets.

Authors contributions

Kerstin Stebel (KS), Philipp Schneider (PS), Tove Svendby (TS), and Arve Kylling (AK) wrote the SAT4AQN final report; KS was responsible for project design, coordination and episode selection; TS performed the WRF-EMEP modeling; PS developed and implemented the downscaling algorithm and performed the downscaling of AOD and PM; AK supplied the review of alternative downscaling techniques; PS, AK and KS contributed to the evaluation of the downscaled data.

References

Atkinson, P. M. (2013). Downscaling in remote sensing. *International Journal of Applied Earth Observation and Geoinformation*, 22:106–114.

Boucher, A. (2009a). Sub-pixel mapping of coarse satellite remote sensing images with stochastic simulations from training images. *Mathematical Geosciences*, 41(3):265–290.

Boucher, A. (2009b). Sub-pixel mapping of coarse satellite remote sensing images with stochastic simulations from training images. *Mathematical Geosciences*, 41(3):265–290.

Breiman, L. (2001). Random Forests. *Machine Learning*, 45(1):5–32.

Burges, C. J. C. (1998). A tutorial on support vector machines for pattern recognition. *Data Mining and Knowledge Discovery*, 2:121–167.

Goovaerts, P. (1997). *Geostatistics for natural resources evaluation*. Oxford University Press, New York.

Goovaerts, P. (2008). Kriging and semivariogram deconvolution in the presence of irregular geographical units. *Mathematical Geosciences*, 40(1):101–128.

Gottschalk, L., Leblois, E., and Skøien, J. O. (2011). Distance measures for hydrological data having a support. *Journal of Hydrology*, 402(3-4):415–421.

Ha, W., Gowda, P. H., and Howell, T. A. (2013). A review of downscaling methods for remote sensing-based irrigation management: Part I. *Irrigation Science*, 31(4):831–850.

Hijmans, R. J. and van Etten, J. (2012). *raster: Geographic analysis and modeling with raster data*.

Ho, T. K. (1998). The random subspace method for constructing decision forests. *IEEE Transactions on Pattern Analysis and Machine Intelligence*, 20(8):832–844.

Im, J., Park, S., Rhee, J., Baik, J., and Choi, M. (2016). Downscaling of AMSR-E soil moisture with MODIS products using machine learning approaches. *Environmental Earth Sciences*, 75(15):1120.

Isaaks, E. H. and Srivastava, R. M. (1989). *Applied geostatistics*. Oxford University Press, New York.

Jensen, R. R., Hardin, P. J., and Yu, G. (2009). Artificial Neural Networks and Remote Sensing. *Geography Compass*, 3(2):630–646.

Ke, Y., Im, J., Park, S., and Gong, H. (2016). Downscaling of MODIS One Kilometer Evapotranspiration Using Landsat-8 Data and Machine Learning Approaches. *Remote Sensing*, 8(3).

Kolios, S., Georgoulas, G., and Stylios, C. (2013). Achieving downscaling of Meteosat thermal infrared imagery using artificial neural networks. *International Journal of Remote Sensing*, 34(21):7706–7722.

Kyriakidis, P. C. (2004). A Geostatistical Framework for Area-to-Point Spatial Interpolation. *Geographical Analysis*, 36(3):259–289.

Myhre, C. L., Svendby, T., Hermansen, O., Lunder, C., Fiebig, M., Hansen, G., Schmidbauer, N., and Krognes, T. (2017). Monitoring of greenhouse gases and aerosols at Svalbard and Birkenes in 2016 – Annual report. *Miljødirektoratet rapport*, M-871/2016 (39/2017).

Pardo-Iguzquiza, E., Atkinson, P. M., and Chica-Olmo, M. (2010). DSCOKRI: A library of computer programs for downscaling cokriging in support of remote sensing applications. *Computers and Geosciences*, 36(7):881–894.

Pardo-Igúzquiza, E., Chica-Olmo, M., and Atkinson, P. M. (2006). Downscaling cokriging for image sharpening. *Remote Sensing of Environment*, 102(1-2):86–98.

Park, N. W. (2013). Spatial downscaling of TRMM precipitation using geostatistics and fine scale environmental variables. *Advances in Meteorology*, 2013.

Pebesma, E. (2018). *sf: Simple Features for R*.

R Core Team (2018). R: A Language and Environment for Statistical Computing.

Simpson, D., Benedictow, A., Berge, H., BergstrÃűm, R., Emberson, L., Fagerli, H., Hayman, G., Gauss, M., Jonson, J., Jenkin, M., NyÃ⬡ri, A., Richter, C., Semeena, V., Tsyro, S., Tuovinen, J.-P., Valdebenito, A., and Wind, P. (2012). The EMEP MSC-W chemical transport model âĂŞ- technical description. *Atmospheric Chemistry and Physics*, 12:7825–âĂŞ7865.

Skamarock, W. C. and Klemp, J. B. (2008). A time-split nonhydrostatic atmospheric model for weather research and forecasting applications. *J. Comput. Phys.*, 227(7):3465–3485.

Skøien, J. O., Blöschl, G., Laaha, G., Pebesma, E., Parajka, J., and Viglione, A. (2014). rtop: An R package for interpolation of data with a variable spatial support, with an example from river networks. *Computers and Geosciences*, 67:180–190.

Skøien, J. O., Merz, R., and Blöschl, G. (2006). Top-kriging - Geostatistics on stream networks. *Hydrology and Earth System Sciences*, 10(2):277–287.

Srivastava, P. K., Han, D., Ramirez, M. R., and Islam, T. (2013). Machine Learning Techniques for Downscaling SMOS Satellite Soil Moisture Using MODIS Land Surface Temperature for Hydrological Application. *Water Resources Management*, 27(8):3127–3144.

Tipping, M. E. (2001). Sparse Bayesian Learning and the Relevance Vector Machine. *Journal of Machine Learning Research*, 1:211–244.

van Donkelaar, A., Martin, R. V., Brauer, M., Kahn, R., Levy, R., Verduzco, C., and Villeneuve, P. J. (2010). Global estimates of ambient fine particulate matter concentrations from satellite-based aerosol optical depth: development and application. *Environmental health perspectives*, 118(6):847–55.

VoPham, T., Hart, J. E., Bertrand, K. A., Sun, Z., Tamimi, R. M., and Laden, F. (2016). Spatiotemporal exposure modeling of ambient erythemal ultraviolet radiation. *Environmental Health*, 15(1):111.

Wackernagel, H. (2003). *Multivariate geostatistics: an introduction with applications*. Springer, Berlin, Heidelberg, New York.

Wilby, R. and Wigley, T. (1997). Downscaling general circulation model output: a review of methods and limitations. *Progress in Physical Geography*, 21(4):530–548.

Wu, C. and Murray, A. T. (2003). Estimating impervious surface distribution by spectral mixture analysis. *Remote Sensing of Environment*, 84(4):493–505.

Zhang, X., Jiang, H., Zhou, G., Xiao, Z., and Zhang, Z. (2012). Geostatistical interpolation of missing data and downscaling of spatial resolution for remotely sensed atmospheric methane column concentrations. *International Journal of Remote Sensing*, 33(1):120–134.

NILU – Norwegian Institute for Air Research

NILU – Norwegian Institute for Air Research is an independent, non-profit institution established in 1969. Through its research NILU increases the understanding of climate change, of the composition of the atmosphere, of air quality and of hazardous substances. Based on its research, NILU markets integrated services and products within analysing, monitoring and consulting. NILU is concerned with increasing public awareness about climate change and environmental pollution.

NILU's values: *Integrity - Competence - Benefit to society*
NILU's vision: *Research for a clean atmosphere*

NILU – Norwegian Institute for Air Research
P.O. Box 100, NO-2027 KJELLER, Norway

E-mail: nilu@nilu.no
http://www.nilu.no

ISBN: 978-82-425-2963-3
ISSN: 2464-3327

Norsk institutt for luftforskning
Norwegian Institute for Air Research